Spatial variability of turbulent mixing from an underwater glider in a large, deep stratified lake

Oscar Sepúlveda Steiner[1,2], Alexander L. Forrest[3,4], Jasmin B. T. McInerney[3], Bieito Fernández Castro[2,5], Sébastien Lavanchy[2], Alfred Wüest[1,2], and Damien Bouffard[1]

[1]Eawag, Swiss Federal Institute of Aquatic Science and Technology, Surface Waters – Research and Management, Kastanienbaum, Switzerland.

[2]Physics of Aquatic Systems Laboratory, Margaretha Kamprad Chair, Institute of Environmental Engineering, ENAC, École Polytechnique Fédérale de Lausanne, Lausanne, Switzerland.

[3]Civil & Environmental Engineering, University of California – Davis, Davis, CA, USA.

[4]UC Davis Tahoe Environmental Research Center, Incline Village, NV, USA.

[5]Ocean and Earth Sciences, National Oceanography Centre, University of Southampton, Southampton, UK

Key Points:

- Underwater gliders are reliable platforms for scanning spatial heterogeneity and estimating turbulent dissipation in large lakes.
- Glider-based temperature microstructure turbulence estimates reveal inhibited mixing in the interior hypolimnion under stratified conditions.
- Centrifugal instabilities are a plausible explanation for augmented turbulent dissipation measured on a gradual coastal slope.

Corresponding author: Oscar SEPÚLVEDA STEINER, oscar.sepulvedasteiner@eawag.ch

Abstract

Spatial variability of physical properties induced by circulation and stirring remains unaccounted for in the energy pathway of inland waters. Recent efforts in microstructure turbulence measurements have unraveled the overall energy budget in lakes. Yet, a paucity of lake-wide turbulence measurements hinders our ability to assess how representative such budgets are at the basin scale. Using an autonomous underwater glider equipped with a microstructure payload, we explored the spatial variability of turbulence in Lake Geneva. Microstructure analyses allowed turbulent dissipation rates and thermal variances estimations by fitting temperature gradient fluctuations spectra to the Batchelor spectrum. In open waters, results indicate mild turbulent dissipation rates in the surface and thermocline ($\sim 10^{-8}$ W kg^{-1}), which weaken towards the deep hypolimnion ($\sim 10^{-11}$ – 10^{-10} W kg^{-1}). The strong thermal stratification inhibited interior mixing in the thermocline. In contrast, measurements along the coastal slope reveal a notorious enhancement of turbulent dissipation ($\sim 5 \times 10^{-8}$ W kg^{-1}) above the sloping topography way above the known extent of the bottom boundary layer. These distinct turbulence patterns result from differing large-scale dynamics in the interior and coastal environments. Current measurements in open waters show dominant internal Poincaré waves. On the coast, three-dimensional numerical results from `meteolakes.ch` suggest that enhanced bottom dissipations arise from the development of centrifugal instabilities. A process driven by coastal cyclonic circulation interacting with the sloping bottom reported for the ocean but so far overlooked in large lakes. The spatially-distributed turbulence measurements we report here highlight the potential of underwater glider deployments for further lake exploration.

Plain Language Summary

Estimating kinetic energy distribution in lakes remains challenging due to a lack of lake-wide turbulence measurements. We show that underwater gliders can address this gap by providing reliable maps of turbulent mixing estimates covering broad areas. Results reveal clear differences in turbulence intensity and mixing between the interior and coastal zones of deep Lake Geneva (Switzerland/France). In the interior, measurements show that (i) turbulence variation happens mainly vertically, and (ii) strong thermal stratification inhibits turbulent mixing much more than expected for such a large windy lake. Glider measurements along the coastal slope, by contrast, mostly show horizontal turbulent variation. Also, the thickness of the bottom frictional zone at the slope, where most energy dissipates, exceeds known values. We propose that centrifugal instabilities are responsible for these intense turbulent dissipation measurements based on numerical simulations. Such interactions between rotating currents and the bottom are known for the ocean but so far overlooked in large lakes. Our findings disclose the distinct turbulence characteristic of the interior and coastal regions and highlight gliders' capability for lake exploration.

1 Introduction

Climate change is modifying the thermal structure of lakes – rising surface water temperatures and strengthening background stratification (Adrian et al., 2009; Sahoo et al., 2016; Schwefel et al., 2016). In a resulting future scenario of diminished vertical transport, ecologically-relevant exchanges such as oxygen and nutrients renewal will rely primarily on three-dimensional (3D) hydrodynamic processes. Yet, the spatial variability of physical properties induced by more complex lake hydrodynamics and in particular its link to energy distribution remains poorly studied. A better understanding of lake-wide turbulent mixing can help connect these interactions and ultimately foster our ability to assess the effects of climate change on lake ecosystems.

The pathway of energy transference across scales, or energy cascade, is a key concept to assess the impacts of atmospheric forcing on the spatial variability of standing water bodies. External forcing transfers energy to large-scale motions providing turbulent kinetic energy (TKE) and inducing spatial variability. Then, TKE cascades to smaller scales until it dissipates by friction, mainly at the boundaries (Imberger, 1998). Turbulence microstructure measurements have unraveled the contributions of the interior and boundary regions for the overall kinetic energy budget in the hypolimnion of lakes (Fernández Castro, Bouffard, et al., 2021; Wüest et al., 2000). However, it is still unknown how representative these budgets are at the spatial extent, particularly for large lakes that exhibit substantial turbulence characteristics differences within a few km distances (e.g., Bouffard et al., 2012; Lemckert et al., 2004). The aim of this work is to provide insight into the spatial distribution of turbulent quantities in lakes' interior and coastal regions using underwater glider measurements (Figure 1).

In medium-to-large lakes, wind and Earth rotation's combined effect are a significant source of spatial variability (Csanady, 1975). Complex basin-scale processes such as coastal upwelling (Reiss et al., 2020; Roberts et al., 2021; Schladow et al., 2004), gyres (Ishikawa et al., 2002; Laval et al., 2005; Shimizu et al., 2007), and rotational internal waves (Antenucci et al., 2000; Appt et al., 2004; Bouffard et al., 2012), drive transport and stirring at a wide range of scales. Consequently, these processes will redistribute energy through the generation of turbulence and mixing. Characterizing the spatial variability ranging from basin-scale processes to small-scale turbulence, in situ, is essential to assess lake-wide energy budgets.

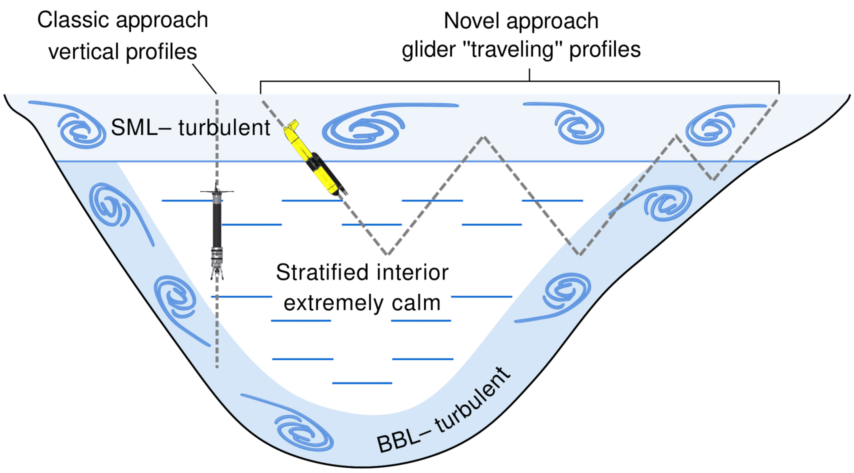

Figure 1. Schematics of turbulence intensity in a stratified lake. The sketch depicts turbulence microstructure measurements from a free-falling profiler and an underwater glider transect.

Spatially distributed measurements are required to characterize the spatial heterogeneity of physical and biogeochemical processes. Manual observations of spatial variability such as Conductivity-Temperature-Depth (CTD) transects (Alexander & Imberger, 2013; MacIntyre et al., 2002, 2014) and piloted submarine-based measurements (Fer et al., 2002; Gargett et al., 1984; Osborn & Lueck, 1985; Thorpe et al., 1999) have successfully been applied. However, these applications are logistically and financially prohibitive. Novel autonomous measuring platforms such as self-propelled Autonomous Underwater Vehicles (AUVs; Forrest et al., 2008; Laval et al., 2000) and underwater gliders (Rudnick, 2016; Webb et al., 2001) enable the coupled scanning of vertical and horizontal gradients of water properties with fewer restrictions. The variety of sensors integrated into underwater vehicles, including CTDs and water quality sensors, makes them a suitable platform for studying spatial variability.

Buoyancy-controlled autonomous underwater vehicles (aka gliders) provide sawtooth transects through the water column with low levels of vibration and mechanical noise (Davis et al., 2002). This feature makes them a suitable platform for turbulence measurements, which require extremely low vibrations. Microstructure-based turbulence estimates using gliders have been tested in deep oceanic environments featuring energetic (Fer et al., 2014; Peterson & Fer, 2014) and weak (Scheifele et al., 2018) regimes as well as in the upper ocean (Lucas et al., 2019) and shallow shelf seas (Schultze et al., 2017). Although the potential for underwater glider deployments in lakes has been previously identified (Austin, 2013), their practical application remains reduced (Austin, 2012, 2019; McInerney et al., 2019) and we still lack clear assessment of the potential of glider-based turbulence observations in lakes.

In the present study, we sought to shed light on the turbulence characteristics of distinct lake regions using an underwater glider. To this end, we first validated temperature microstructure turbulence estimates from a moving platform in a weakly energetic system. With this technical barrier solved, we present a large and novel dataset of glider-based turbulent mixing in the interior and coastal regions of a large, deep stratified lake. We carry out two analyses of turbulent mixing. First, we use the lake interior results (five [5] missions) to evaluate turbulent mixing parameterizations in this region and discuss particular aspects of strongly stratified and weakly energetic systems. Second, we focus on the interior-coast transition region, where our measurements revealed a striking turbulent dissipation enhancement (one [1] mission). Based upon the results of an operational 3D lake forecast model (`meteolakes.ch`; Baracchini et al., 2020), we present a discussion of a possible hydrodynamic process driving this enhanced dissipation in a specific coastal region of Lake Geneva.

2 Study site

This study was conducted on Lake Geneva (*Lac Léman*; Figure 2), a deep (309 m max. depth) and large (582 km^2 surface area) perialpine lake located between Switzerland and France. Lake Geneva is the largest natural freshwater body in Western Europe and is classified as a warm-monomictic lake where complete deep winter mixing seldomly occurs (Schwefel et al., 2016). During the seasonal stratification, the thermocline is located at $\sim$5 to $\sim$10 m depth in May and gradually deepens during summer and autumn before deep winter convective mixing sets in. The wind is the driving force for horizontal water mass movements (Bohle-Carbonell, 1986), exhibiting two dominant winds: North-East (*La Bise*) and South-West (*Le Vent*; Lemmin & D'Adamo, 1996). Previous studies highlighted the role of Coriolis in the dynamics of Lake Geneva (Bauer et al., 1981; Lemmin et al., 2005; Reiss et al., 2020). Particularly during summer stratified conditions, when the maximum width of the lake ($\sim$14 km) is more than three times larger than the internal Rossby radius ($\sim$4 km; Bouffard & Lemmin, 2013a), this rotational effect modifies the circulation and stirring in the lake. Past studies of turbulence in Lake Geneva have mainly focused on the near-shore region. Cooling-driven gravity currents (Fer et al., 2002) and internal Kelvin wave-induced shear (Bouffard & Lemmin, 2013b; Thorpe et al., 1999) cause localized and intermittent enhancements of turbulent dissipation. In the lake interior, Michalski and Lemmin (1995) used bulk methods (e.g., Jassby & Powell, 1975) to estimate diffusivity from monthly temperature profiles, finding well above molecular levels (i.e., turbulent mixing) in the upper hypolimnion (down to ∼90 m depth). Instantaneous microstructure turbulence measurements in this zone, up to date, have not been reported.

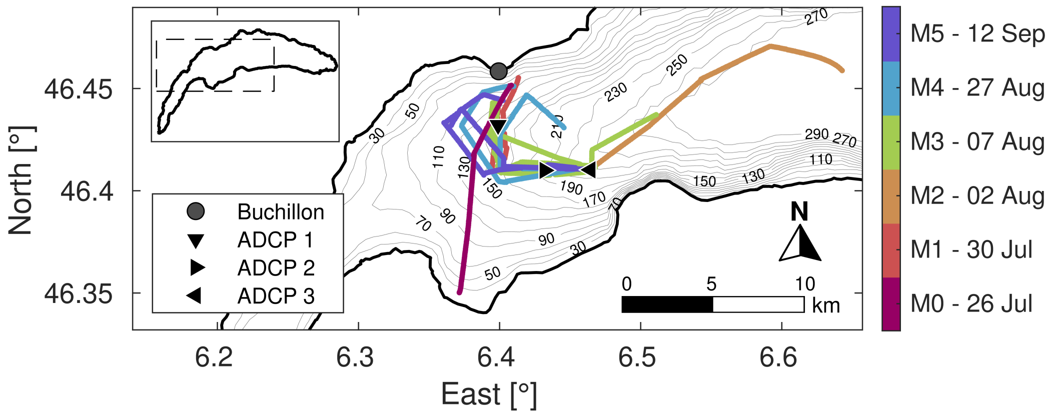

Figure 2. Study site location. Bathymetry of Lake Geneva with the location of the Buchillon station and the three moorings (ADCP 1 to 3). Color-coded lines depict glider missions M0 to M5, respectively. Dates correspond to the year 2018.

3 Materials and methods

3.1 Slocum glider and turbulence package

We performed spatially distributed measurements in Lake Geneva using the UCDavis glider *Storm Petrel*, a G2 Slocum underwater glider (1000 m depth; Teledyne Webb Research). During our sampling campaigns, the glider payload included a Sea-Bird pumped CTD, Sea-Bird ECO Puck measuring Chlorophyll-a fluorescence and an Aanderaa Optode dissolved oxygen (DO) sensor. Additionally, a MicroRider-1000 turbulence package (Rockland Scientific Canada) mounted on top of the glider (Fer et al., 2014) recorded microstructure turbulent fluctuations. This customized instrument included two shear and two temperature microstructure channels, an inclinometer, and an accurate pressure sensor sampling at 512 Hz. The glider with the mounted MicroRider was ballasted in a freshwater pool with water density comparable to lake water.

3.2 Measurements

3.2.1 Glider transects

Interior – Our glider missions were carried out in the western part of the main basin to minimize safety hazards with summer boat activity offshore of Lausanne. The sampling strategy consisted mainly of repeated L-shaped trajectories keeping the glider away from the steep Northern-shore bathymetry (Figure 2). The glider was programmed to perform continuous dives and climbs (downcast and upcast profiles, respectively) between 3 and 100 m depth, reaching the surface every 4 h for communication and GPS position update. The profiling was programmed to reach 100 m depth for navigation safety and data quality purposes. Although a deep glider (1000 m depth) is slow at turns, the adopted sampling strategy enables a smooth passage through a significant portion of the water column representing a great range of variability and ensures that inflexions of the glider occur far away from the thermocline. We programmed the glider to perform flights with a fixed pitch angle, which allows for battery position adjustments throughout the missions. Still, the battery position remained almost constant during each dive and climb, therefore not interfering with the flight behavior. For this mission design, the glider traveled a distance of $\sim$410-450 m between two dives and performed 9 to 10 yoyos (dive and climb) during the 4 h immersion period.

Coastal transition – An opportunistic mission from Buchillon towards the Southern shore of the lake (M0; Figure 2) allowed us to traverse a gentle slope into the coastal region. The vehicle's flight parameters were the same as for the interior missions. In particular, the bottom detection system (underwater altimeter) was set with a tolerance of 10 m to the bottom, allowing the glider to adjust maximal dive depth when approaching zones shallower than 100 m.

3.2.2 Microstructure measurements

We collected temperature and shear microstructure measurements during our sampling. The focus in this study is on the foremost for two reason: firstly, turbulence estimates based on the temperature microstructure technique have shown better performance than shear to characterize weak turbulence, as typically encountered in the stratified hypolimnion of lakes (Kocsis et al., 1999) and occasionally in strongly stratified zones of the ocean (Scheifele et al., 2018); secondly, shear microstructure measurements were not always available due to probes damage during vehicle encounters with fishing nets. Still, the online dataset includes all microstructure measurements for reproducibility and open science purposes (see Data Availability Statement). A substantial amount of turbulence research in lakes (e.g., Bouffard & Boegman, 2013; Imberger & Ivey, 1991; Saggio & Imberger, 2001; Wüest et al., 2000) sustains our choice to proceed with temperature microstructure only.

3.2.3 Wind and current measurements

A hydro-meteorological station located at Buchillon (Figure 2) provided wind speed and direction measurements from a 05103 Wind Monitor anemometer (Young, USA) installed at 10 m above the water level, and sampling means and gust values every 10 mins. We performed current velocity profiles measurements using Acoustic Doppler Current Profilers (ADCPs) to complement the glider observations with background hydrodynamic information. The deployment comprised three suspended upward-looking ADCPs installed in the open water region (Figure 2), in addition to a long-term deployment of a bottom-moored upward-looking ADCP at Buchillon station. Installation of ADCP moorings 1 to 3 consisted of lines equipped with subsurface floaters at their uppermost end ($\sim$50 m depth). Each ADCP was installed within a frame assembled to the line, 5 m below the floater (assuring no signal interference). An acoustic releaser system was also installed at the bottom to retrieve the instruments. This setup allowed scanning the upper part of the water column with a reasonable resolution given the local restriction due to professional fishing in the top 50 m. Table 1 lists ADCPs information and deployment depths.

3.3 Flight model

Glider along-path speeds (U) are required to perform accurate turbulence estimations. These are used to treat the microstructure data with the Taylor frozen-flow hypothesis (section 3.4). Nevertheless, the vehicle's speed through water cannot directly be obtained from instrumentation commonly mounted on gliders and *Storm Petrel* is no exception. To address this lack of data, we implemented an underwater glider flight model (Frajka-Williams et al., 2011; Merckelbach et al., 2010). Specifically, we used the dynamic flight model of

Table 1. Details of instruments deployed on each station (Figure 2). Each station was equipped with a Teledyne RD Workhorse Sentinel of the specified frequency. ADCPs 1 to 3 were installed from 25 July to 10 October 2018.

Station	Frequency [kHz]	Ensemble interval [min.]	Installation depth [m]	Bin size [m]
Buchillon	600	15	38	0.75
ADCP 1	600	10	50	1.0
ADCP 2	600	10	42	1.0
ADCP 3	300	5	46	1.0

Merckelbach et al. (2019). Details of the implementation are presented in the Supporting Information (SI; Text S1 and Figure S1).

3.4 Turbulence estimations and mixing quantities

3.4.1 Turbulent dissipation from temperature microstructure

The possibility to estimate turbulence from temperature microstructure sensors (fast thermistors) mounted on gliders has already been successfully demonstrated (Peterson & Fer, 2014; Scheifele et al., 2018). Measurements carried out with these sensors can be used to estimate rates of turbulent kinetic energy dissipation ε (W kg^{-1}) by fitting the measured temperature gradient spectra (S_{obs}) to a theoretical spectral shape $S = S(k_C, \chi_\theta)$, as a function of a cutoff wavenumber (k_C) and the smoothing rate of temperature variance, χ_θ (°C^2 s^{-1}).

Here, we adjust S_{obs} to the Batchelor (1959) spectrum, S_B, to extract turbulence information from the microstructurecutre data. Performing such spectral fitting allows us to infer ε estimates because the Batchelor cutoff wavenumber, k_B (cpm), is defined as a function of ε by:

$$k_B = \frac{1}{2\pi}\left(\frac{\varepsilon}{\nu D_T^2}\right)^{\frac{1}{4}} \tag{1}$$

where $\nu \approx 1.5 \times 10^{-6}$ m^2 s^{-1} is the kinematic viscosity and $D_T = 1.4 \times 10^{-7}$ m^2 s^{-1} is the molecular thermal diffusion coefficient at hypolimnion temperatures. This data processing employs the maximum likelihood spectral fitting method (Ruddick et al., 2000) to estimate ε, coupled with the Steinbuck et al. (2009) approach to calculate χ_θ.

The first step of the procedure is to obtain S_{obs}. To do so, the fast thermistors data are first treated with a frequency response correction following Sommer et al. (2013). Afterward, the data processing is similar to the methodology of Scheifele et al. (2018). However, we use half-overlapping microstructure temperature segments of 10 s to calculate frequency spectra instead of 40 s. This data treatment allows us to maximize the amount of S_{obs} for turbulence analysis without compromising data quality (see section 4.2).

Then, the procedure requires obtaining χ_θ. Here we take advantage of the Steinbuck et al. (2009) correction to filter fine-scale fluctuations (Gregg, 1977) and possible low-frequency vehicle-induced contamination by modifying some commonly used parameters (namely k_l and k_u in Eq. 2). The calculation of χ_θ is performed with the following integral:

$$\chi_\theta = \chi_l + \chi_{obs} + \chi_u = 6D_T\left(\int_o^{k_l} S_B\,dk + \int_{k_l}^{k_u} (S_{obs} - S_n)\,dk + \int_{k_u}^{\infty} S_B\,dk\right) \tag{2}$$

with the factor 6 for assuming isotropy. The lower wavenumber end of the measured spectra (k_l) is obtained by considering k_l =max{first $k_{obs} > 0$; $3k_*$}, where $k_* = 0.04 k_B (D_T/\nu)^{1/2}$ is the so-called transitional wavenumber separating the inertial and viscous-convective subranges (Dillon & Caldwell, 1980). Whereas the upper wavenumber end (k_u) is the intersection of S_{obs} with the noise spectra S_n. Outside the range defined by k_l and k_u, given the lack of reliability of S_{obs}, Steinbuck et al. (2009) propose to use the theoretical expression of S_B to obtain the fringe contributions of χ_l and χ_u.

By coupling the estimation of χ_θ and S_B and solving iteratively for k_B, we can finally obtain ε. Turbulence analyses exclude data collected 5 m within turning points as these present diminished data quality from vibrations and may not satisfy the Taylor frozen-flow hypothesis (Fer et al., 2014). Dissipation estimates obtained from poorly resolved spectra, which do not comply with the Bachelor fitting, are discarded following the likelihood and mean absolute deviation criteria Ruddick et al. (2000) proposed. For temperature microstructure, the detection floor of ε is in the range of 10^{-12} to 10^{-11} W kg^{-1} (Luketina & Imberger, 2001; Steinbuck et al., 2009).

Turbulent quantities often exhibit lognormal character. Statistical analyses, therefore, used the maximum likelihood estimator (mle) for lognormal distributions (Baker & Gibson, 1987). This approach reduces the influence of extreme values and provides ad-hoc estimates of statistical variability through the intermittency factor $\langle \sigma^2_{mle} \rangle$, which is denoted by pointy brackets, $\langle \cdot \rangle$, throughout the article.

3.4.2 Turbulent mixing characteristics

Mixing is quantified using χ_θ by following the Osborn and Cox (1972) diapycnal diffusivity model, defined as:

$$K_T = \frac{\chi_\theta}{2\left(\frac{\partial \overline{T}}{\partial z}\right)^2} \tag{3}$$

where $\partial \overline{T}/\partial z$ is the background temperature gradient, obtained by calculating the slope of T in the vertical segment of interest through linear regression.

We use the isotropic version of the Cox number to quantify the turbulent to molecular vertical mixing ratio, defined as (Thorpe, 2007):

$$C_x = 3\frac{\left(\frac{\partial T'}{\partial z}\right)^2}{\left(\frac{\partial \overline{T}}{\partial z}\right)^2} = \frac{K_T}{D_T} \tag{4}$$

where $\partial T'/\partial z$ is the temperature fluctuation gradient. This also accounts for the strength of turbulent fluctuations compared to the background temperature gradient. We use directly K_T obtained from Eq. (3) to compute Cox numbers.

To account for mixing efficiency, we use the flux Richardson number (Ri_f; Monismith et al., 2018). Assuming steady and homogeneous turbulence, the local shear production (P) balances with the sum of buoyancy flux and dissipation (i.e. $P = B + \varepsilon$; Ivey & Imberger, 1991). Hence, we can define Ri_f as:

$$Ri_f = \frac{B}{B + \varepsilon} \tag{5}$$

where $B = K_T N^2$ is the buoyancy flux and $N^2 = g\rho_o^{-1}\partial\rho/\partial z$ is the water column stability, $g = 9.81$ m s^{-2} and z is the depth coordinate (positive downwards). Freshwater density, ρ, is calculated from CTD data using methods ad-hoc with TEOS 2010 (McDougall & Barker, 2011) and $\rho_o = 1000$ kg m^{-3} is the freshwater reference density. The density gradient, $\partial\rho/\partial z$, is obtained through linear regression of ρ in the vertical segment of interest.

To characterize the intensity of turbulence with respect to stratification, we use the buoyancy Reynolds number (Gibson, 1980):

$$Re_b = \frac{\varepsilon}{\nu N^2} \tag{6}$$

which defines three energy regimes (Ivey et al., 2008): molecular ($Re_b < 7$), transitional ($7 < Re_b < 100$) and turbulent ($Re_b > 100$).

3.5 Horizontal kinetic energy

We use the ADCP current data to determine the depth-integrated horizontal kinetic energy (HKE), as follows:

$$\mathrm{HKE} = \frac{1}{2}\int_0^{z_{\mathrm{ADCP}}} (u^2 + v^2)\ dz \quad (\mathrm{m}^3\ \mathrm{s}^{-2}) \tag{7}$$

where u and v are the East and North current components, respectively. The vertical integration range is considered from the surface ($z = 0$ m) to $z_{\mathrm{ADCP}} = 40$ m depth. An approximation of the characteristic radius resulting from current-induced circulation at a specific frequency band (f^*) can then be defined as:

$$R^* = \frac{\sqrt{2\overline{\mathrm{HKE}^*} z_{\mathrm{ADCP}}^{-1}}}{2\pi f^*} \tag{8}$$

where $\overline{\mathrm{HKE}^*}$ is the mean of the f^*-bandpass filtered HKE.

4 Results

This research explores the capabilities of underwater gliders for studying spatial variability in a large lake. Glider *Storm Petrel* was deployed in Lake Geneva in the summer of 2018 to connect large-scale spatial variability to turbulence activity. Throughout the six missions considered in this study, we measured 345 yo-yo sets equivalent to 155 h of sampling, covering a lake surface distance of 158 km. Next, we present an overview of the data collected by the glider, a turbulence estimate assessment, a comparison of turbulence and mixing conditions between interior and coastal regions of the lake, and the sources of spatial variability evaluated from wind and ADCP measurements.

4.1 Glider measurements

Interior – We show a time-series example of data collected during mission M2 (Figures 3a,b), consisting of a long transect through the middle of the lake (Figure 2). This and the other interior missions, accompanied by water quality parameters less relevant for the analysis presented herein (namely Chlorophyll-a and dissolved oxygen), are presented in the SI (Figures S2-S6). Mission-composite averaged profiles during M2 show a marked vertical structure (Figures 3c,d). Temperature data show a strong vertical stratification (Figure 3c). However, a more careful analysis of the transect reveals lateral heterogeneity in the top 50 m with varying thermocline depths (depicted by ~ 15°C isotherm; Figures 3a,b). The first 4 h of this mission presented colder temperatures close to the surface, suggesting a thermocline uplift in the eastern part of the main basin. Although presenting a vertically consistent decay (Figure 3d), fast temperature gradients exhibit horizontal variability with sharper gradients in the upper water column (Figure 3b). Considering abs(T grad.)> 0.4 °C m^{-1} as a proxy for the thermocline, the gradient time-series indicates two thermocline uplift regions (at the beginning of the mission and around 2 Aug 2018 – 18:00; Figure 3b). Similar yet subtle spatio-temporal variability was observed during other missions (see Figures S2-S6).

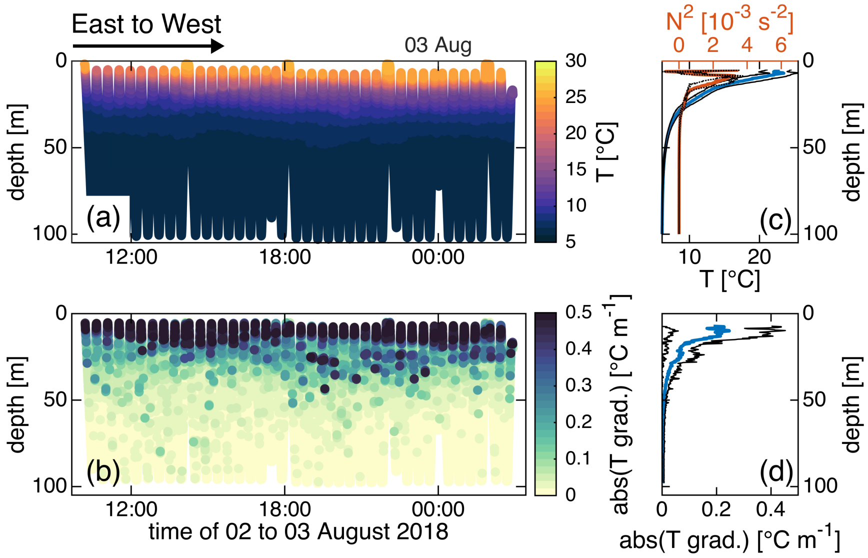

Figure 3. Example of lake-interior glider data collected on 2-3 August 2018 during mission M2. (a) Temperature (T). (b) Absolute value of the temperature gradient measured with the MicroRider, sub-sampled at 4 Hz for visualization. Time increase corresponds to E-W direction (Figure 2).(c-d) Time-averaged profiles (blue lines) of measurements presented in (a-b), accompanied by their respective standard deviations (black line envelopes). Additionally, (c) shows the depth-averaged stability (N^2) profile for mission M2 (red line) with its standard deviation (black dotted envelope).

Coastal transition – The time series of the cross-shore mission M0 (Figures 4a,b) shows similar temperature characteristics as M2. However, the fast temperature gradient structure shows marked spatial heterogeneity with an enhancement toward the slope. Averaged profiles (Figures 4c,d) depict a similar vertical structure as the pelagic profiles with a strong vertical stratification (Figure 3c). Overall, M0 shows a stratified water column with enhanced variability towards the shore, highlighting the different characteristics between the interior and coast. Enhanced temperature gradient fluctuations at the slope suggest a flow-bathymetry interaction. Details of the water quality parameters collected during M0 are presented in Figure S7.

4.2 Turbulence estimates assessment

To evaluate the microstructure analysis methodology for ε and χ_θ estimates, we performed a statistical assessment of the non-dimensional spectral shapes for temperature fluctuations following Dillon and Caldwell (1980). Here, we examine spectra from dives and climbs combined, while separated analyses are presented in the SI (Figures S8, S9). This analysis considers spectra calculated from each fast thermistor as separate samples (no averaging). Figure 5 shows ensemble averages of microstructure temperature gradient spectra treated with the procedure described in section 3.4 that meet the Ruddick et al. (2000) criteria and compare them with S_B for different Cox number (C_x) ranges. Considering measurements 5 m away from the glider's vertical turning points, 60 % of the 91,454 spectra analyzed were non-compliant with this criterion and therefore discarded. For small C_x, i.e., when the background temperature gradients are more prominent than those imposed by turbulent fluctuations, spectra present a shape seemingly in disagreement with the Batchelor form in the lower wavenumber range. For wavenumbers above the spectral maximum, observed spectra show, in general, good agreement with S_B. This resemblance is evident for a wide range of C_x, namely $C_x > 0.1$ (Figure 5c-f).

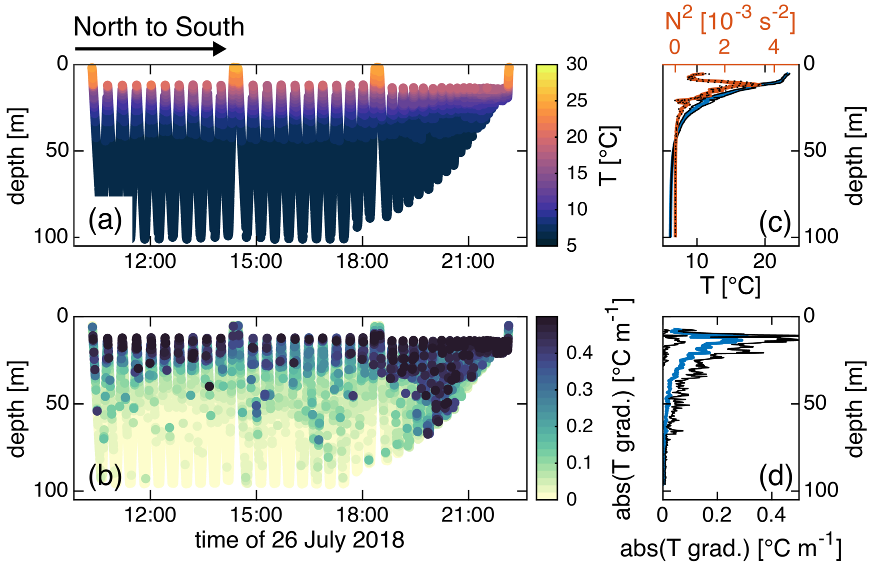

Figure 4. Cross-shore (interior-to-coast) glider data collected on 26 July 2018 during mission M0. Panels are analogous to Figure 3.

The specific evaluation of our procedure to calculate χ_θ (Eq. 2), requires a careful analysis of the S_{obs} ensembles at their wavenumber extremes (Figure 5). At the upper wavenumber end, the intersection of S_{obs} with S_n defines the cutoff and the maximum likelihood method (Ruddick et al., 2000) prevents an overestimation of χ_θ by avoiding the noise-dominated region. For low wavenumbers, the ensemble averages detach from the theoretical form, S_B, possibly due to vehicle-induced vibrations and or stratification fine-scale structures. This deviation becomes more evident at the lower wavenumber end of the spectra for $C_x < 10$ (Figures 5a-d). However, the variance-preserving spectra (circles in Figure 5) show that the statistical variability introduced by S_{obs}, not complying with the theoretical S_B shape, affects only wavenumbers below $3\alpha_*$ (where α_* is the non-dimensional form of k_*) for $C_x < 0.1$ and it is therefore filtered out. These results hold for separated dive and climb analyses (Figures S8, S9). Figure 5 thus shows that our Batchelor spectra fitting procedure performs overall reliably, capturing temperature gradient variance at the relevant wavenumber range, and resulting turbulence quantities can be trusted.

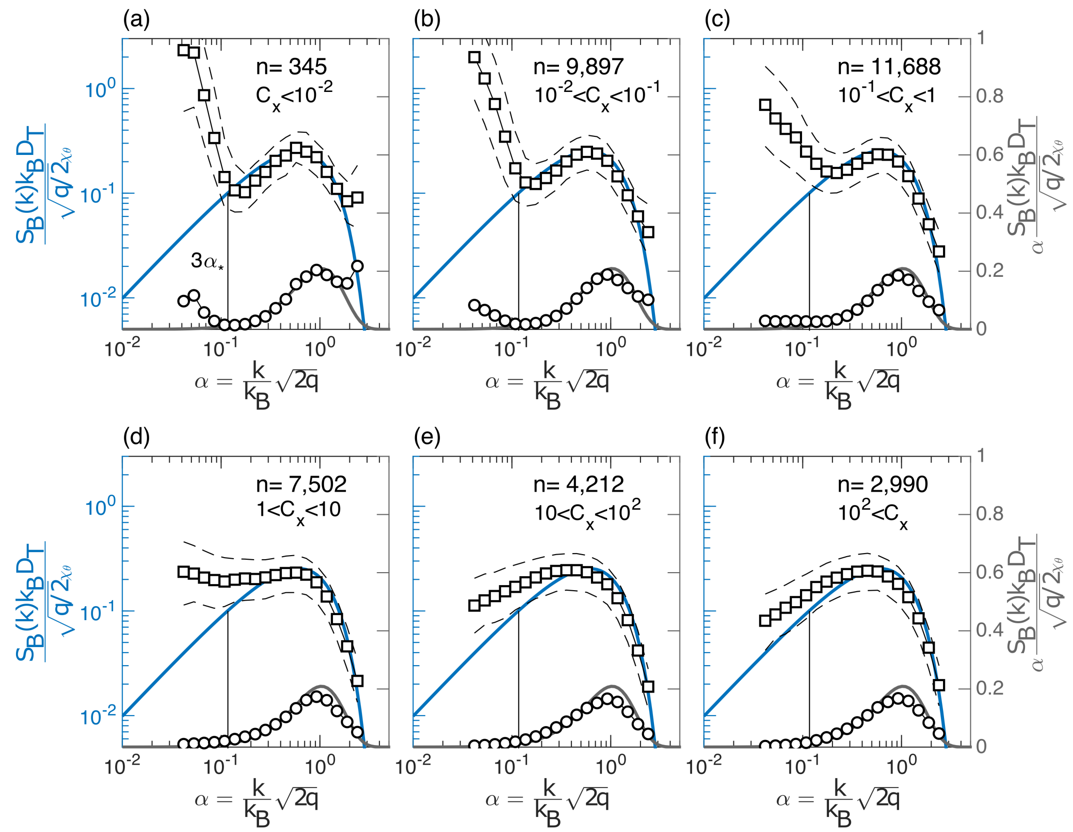

Figure 5. Spectral statistics following Dillon and Caldwell (1980). (a-f) The left y-axis corresponds to ensemble-averaged non-dimensional spectrum (squares) as a function of the non-dimensional wavenumber, α, for Cox numbers (C_x) specified in the top right corner of each panel. This analysis considers spectra meeting the Ruddick et al. (2000) criteria from all missions (including both dives and climbs), with n indicating the number of evaluated spectra. Dashed envelope represent 25$^{\text{th}}$ and 75$^{\text{th}}$ percentile confidence intervals, respectively. The blue line is the non-dimensional Batchelor spectrum $\frac{S_B(k)k_B D_T}{\sqrt{(q/2)}\chi_\theta}$, where $q = 3.4$ is the universal spectral constant. The value $\alpha_* = 0.04\sqrt{\frac{D_T 2q}{\nu}} \approx 0.03$ (vertical black lines) corresponds to the non-dimensional form of the transitional wavenumber k_*. The right y-axis corresponds to the variance-preserving plot of ensemble-averaged non-dimensional spectrum (circles) presented in the left y-axis. Gray line is the variance-preserving non-dimensional Batchelor spectrum $\alpha\frac{S_B(k)k_B D_T}{\sqrt{(q/2)}\chi_\theta}$.

4.3 Turbulence and mixing: Comparison between interior and coastal slope

4.3.1 Statistical and vertical distribution of turbulent quantities

Using the methods described in section 3.4.1, we obtained turbulent dissipation (ε) and temperature variance smoothing rates (χ_θ) for all glider missions (Figure 6 and Table 2). Here, the analysis considers averages of the estimates compliant with the procedure from the twin fast thermistors. We discarded 47% of (averaged) estimates and refer to those considered here as samples. Examinations presented in this section concern dives and climbs combined, while separated analyses are presented in Figure S10 (SI).

For the lake interior, distributions of turbulent quantities (22,762 samples) appear log-normal; however, their log-data kurtosis was 2.4 for ε and 3.6 for χ_θ, distant from the expected value of 3 (lognormal distribution kurtosis). The mle-mean $\langle$intermittency factor$\rangle$ and median for ε were 2.0×10^{-8} W kg^{-1} $\langle 9.8\rangle$ and 9.8×10^{-11} W kg^{-1}, respectively. Whereas for χ_θ the mle-mean and median were 5.7×10^{-8} °C^2 s^{-1} $\langle 10.7\rangle$ and 1.8×10^{-10} °C^2 s^{-1}, respectively. These results indicate overall weak-to-moderate turbulence. Distributions of the interior-to-coast mission (M0; Figures 6b,d) show similar characteristics, although high levels of turbulence were more frequent. Considering 2,368 samples, the log-data kurtosis of M0's turbulence estimates was 2.3 for ε and 2.6 for χ_θ. Dissipation rates for M0 were in the same range as in the interior (M1-M5), with mle-mean and median ε values of 2.6×10^{-8} W kg^{-1} $\langle 8.6\rangle$ and 3.5×10^{-10} W kg^{-1}, respectively. Temperature variance smoothing rates were, however, one order of magnitude larger for M0 than for the interior, with 2.5×10^{-7} °C^2 s^{-1} $\langle 10.7\rangle$ and 1.2×10^{-9} °C^2 s^{-1}. Probability density distribution comparisons of the subsets considered for ε and χ_θ are presented in Figures 6c and 6f.

High dissipation values appear correlated with strong stratification. The stability (N^2) color code indicates a marked concentration of samples obtained under strong stratification on the higher end of ε and χ_θ histograms (Figures 6a,b,d,e). These N^2 values correspond to the upper part of the water column (Figure 7), and considering the upper 20 m ($\sim 40\times10^{-5}$ s^{-2}) as a threshold, both sets present 18.8 % of samples with a strong background stratification. We also analyze the different sections of the water column, namely the epilimnion (surface layer), metalimnion (thermocline), and hypolimnion of the whole dataset to explore this dissipation response to stratification (Figures 6c,f and Table S1 second row). The metalimnion is defined here as the depth range where N^2 exceeds a value of 200×10^{-5} s^{-2}. Epi- and metalimnion combined exhibit ε mle-means two orders of magnitude larger than in the hypolimnion, which reduces to one order of magnitude when considering the median. For χ_θ, the same comparison results in two orders of magnitude difference for both estimators. This N^2-ε dependence is further sustained by a positive linear relation in log-log space when combining all missions samples ($\log_{10}(\varepsilon/\varepsilon_{median}) = \log_{10}(N^2/N^2_{median}) - 0.17$; $R^2 = 0.74$ and p-value ≈ 0).

Vertical distributions (Figures 7 and S11) show an overall decay of ε and χ_θ with depth. The N^2 color code reveals maximal values of ε in the zone of sharper gradients (i.e., maximal N^2). For measurements in the interior (Figure 7a), dissipation shows an increase when approaching 100 m depth. We attribute this to glider flight maneuvers close to its maximal mission depth (100 m), and measurements performed closer to the lake's Northern steep coastal region (see Figure 2), which may present enhanced turbulent dissipation due to its proximity to the bottom. This last characteristic is evident for measurements performed adjacent to the sloping topography during M0 (Figure 7b), which show more significant variability throughout the water column.

When analyzing turbulence estimates from dives and climbs separately (Figure S10 and Table S1, first row), probability distributions have a good resemblance and differ overall by a factor of 5 for ε and 2 for χ_θ regarding mle-means (1.5 for both in terms of median). Similarly, depth-averaged vertical profiles (Figures S10b,e) also show good agreement. Figure S10b indicates that for ε dives and climbs, the main discrepancies locate below the thermocline

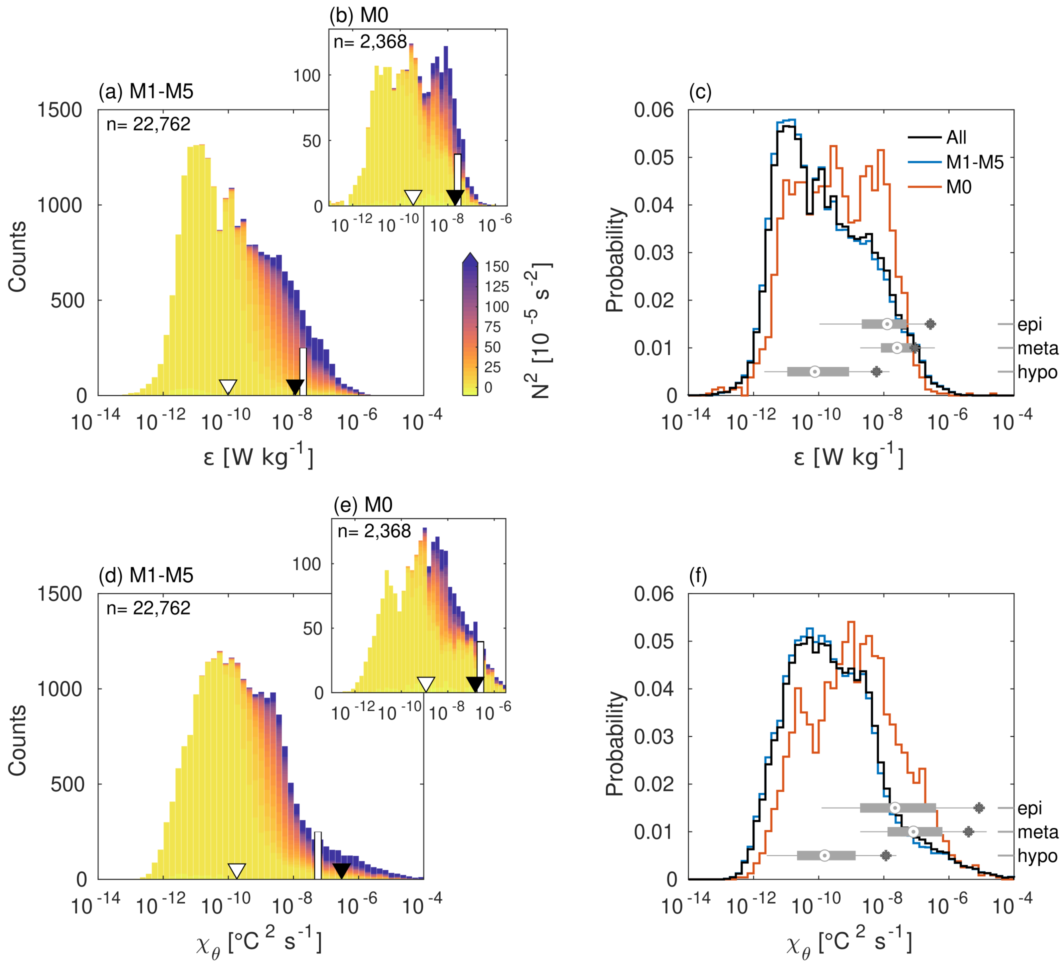

Figure 6. Statistics of measured turbulent characteristics. (a, b) Histograms of turbulent dissipation ε grouped for lake interior (M1-M5) and interior-to-coast transition (M0), respectively, and color-coded for water column stability (N^2). White vertical bars correspond to the mle-mean for a log-normal distribution (Baker & Gibson, 1987), while white and black triangles represent the median and arithmetic mean, respectively. (c) Probability distributions of ε for the whole data set ("All") as well as for the sub-sets described in (a) and (b), accompanied by boxplots of the distinct stratified water column layers, namely: epilimnion, metalimnion (containing the thermocline), and hypolimnion. Boxplots depict median values (dotted circles) with vertical bars and lines representing the 25/75th and 5/95th percentiles, respectively. Asterisks depict mle-means. The calculations consider the metalimnion as the water column portion exceeding $N^2 = 1.5 \times 10^{-3}\ s^{-2}$, with the epi- and hypolimnion the volumes above and below, respectively. (d, e, f) Analogous statistics as in (a, b, c) for the smoothing rate of temperature variance χ_θ. The analysis considers only estimations that meet the Ruddick et al. (2000) criteria. Displayed data points were obtained by averaging the two estimates from the twin fast thermistors mounted on the MicroRider. Data segments with only one sample meeting the criteria were also considered.

Table 2. Statistical summary of the measured turbulent characteristics. Results are reported threefold: (i) mle-mean for lognormal distribution following Baker and Gibson (1987) accompanied by its intermittency factor $\langle \sigma^2_{mle} \rangle$, (ii) median values with its respective 25th and 75th quantiles, and (iii) arithmetic mean ($\overline{x}$) $\pm$ standard deviation (std).

Parameter	Estimator	M1-M5	M0	All
	mle-mean $\langle \sigma^2_{mle} \rangle$	2.0 $\langle 9.8 \rangle$	2.6 $\langle 8.6 \rangle$	2.1 $\langle 9.7 \rangle$
ε [10^{-8} W kg^{-1}]	median [25^{th}, 75^{th}]	0.010 [0.0012, 0.15]	0.035 [0.0033, 0.40]	0.011 [0.0013, 0.17]
	$\overline{x} \pm$ std	1.1 $\pm$ 7.5	2.1 $\pm$ 58.0	1.2 $\pm$ 19.2
	mle-mean $\langle \sigma^2_{mle} \rangle$	5.7 $\langle 10.7 \rangle$	25.4 $\langle 10.7 \rangle$	7.2 $\langle 10.9 \rangle$
χ_θ [10^{-8} °C^2 s^{-1}]	median [25^{th}, 75^{th}]	0.018 [0.0024, 0.19]	0.12 [0.011, 1.1]	0.021 [0.0026, 0.23]
	$\overline{x} \pm$ std	30.1 $\pm$ 586.6	15.3 $\pm$ 135.8	28.7 $\pm$ 559.8

and close to the maximal mission depth. This suggests that buoyancy-induced changes in the vehicle's velocity, either induced by the water column or by the vehicle navigation, affects estimates reliability. Yet, Q-Q plots comparing distributions of ε and χ_θ by stratification range indicate that the agreement between dives and climbs is overall acceptable (Figures S10c,f). This result agrees with glider-based temperature microstructure observations in strongly stratified oceanic waters by Scheifele et al. (2018), who reported no significant ε estimations differences between dives and climbs.

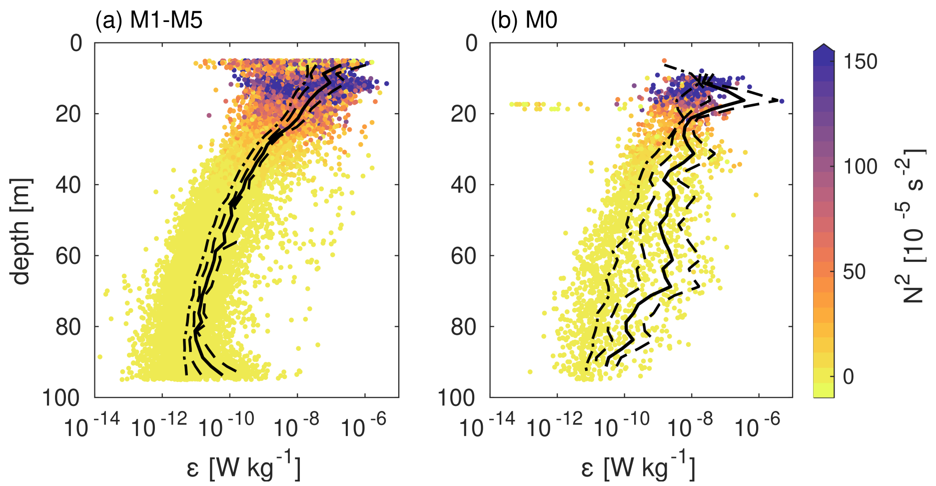

Figure 7. Vertical distribution of measured turbulent dissipation. (a) Interior (M1-M5) and (b) interior-to-coast transition (M0). Thick black line and dashed envelope correspond to the mle-mean and statistical variability given by the intermittency factor, respectively. The dot-dashed line represents the median. Data selection criteria is the same as in Figure 6.

4.3.2 Turbulent mixing

We present depth-averaged vertical profiles to analyze the mixing characteristics of the water column for the two regions (Figure 8). In the interior, all three mixing parameters show maximal values in the epilimnion (Figure 8a-c), a zone usually directly influenced by wind forcing. Vertical profiles of C_x and Ri_f (Figures 8a,b, respectively) present minimum values around 20 m depth. The vertical profile of Re_b (Figure 8c) shows that the water column lies almost entirely within the transitional regime ($7 < Re_b < 100$). Figures 8a-c show that the strong stratification inhibits mixing ($C_x < 1$, $Ri_f < 0.1$, and $R_b < 30$) between 10 and 40 m depth which comprises the thermocline region. This result is similar to that reported by Fernández Castro, Sepúlveda Steiner, et al. (2021) for deep Lake Zurich during stratified conditions.

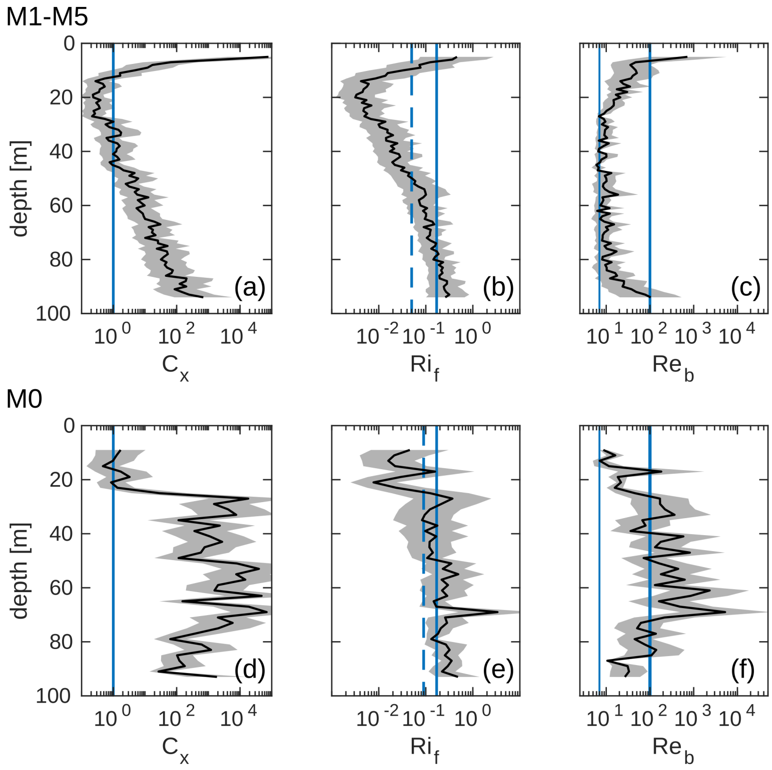

Figure 8. Average profiles of mixing quantities. (a-c) Lake interior (M1-M5) mle-mean profiles (black lines) of C_x, Ri_f and Re_b, respectively. Gray areas in (a-c) represent statistical variability given by the intermittency factor $\langle \sigma^2_{mle} \rangle$. The blue line in (a) is $C_x = K_T D_T^{-1} = 1$. The continuous blue line in (b) represents the canonical oceanic mixing efficiency $Ri_f = 0.17$ (Osborn, 1980). In (c), thin and thick blue lines depict the lower and upper limits of the transitional regime ($7 < Re_b < 100$; Ivey et al., 2008). (d-f) Analogous to (a-c) for the interior-to-coast transition (M5). Dashed lines in (b) and (e) show medians of Ri_f, satisfying $C_x > 1$ and $1 < Re_b < 1000$, in the interior ($Ri_f = 0.05$) and interior-to-coast transition ($Ri_f = 0.09$), respectively.

Conversely, for the interior-to-coast data, the Cox number profile (Figure 8d) clearly shows that in the thermocline region, temperature gradient fluctuations overcome the background stratification, with higher Ri_f values (Figure 8e) and a transitional-to-turbulent energetic regime (Figure 8f). Yet, M0 depth-averaged profiles show minimal values for the three mixing parameters at depths depicting strong stratification (see also Figure 7b), which agrees with observations in the interior. The more consistent vertical structure of the interior profiles compared with those in the interior-to-coast mission can be attributed to (i) the large difference in the number of samples per depth considered (five versus one mission) and (ii) the boundary condition imposed by the lake bathymetry that is likely to result in current-slope interactions driving enhanced turbulence and variability. Altogether the interior shows weak turbulent mixing, which increases when approaching the coast.

4.4 Enhanced dissipation towards the coastal slope

Unlike the more uniform interior estimates of dissipation (M1-M5; Figures 7a), M0 shows a scattered distribution (Figure 7b). To better understand the differences between interior and littoral regions, we present turbulent dissipation estimates for M0 as a transect (Figure 9a). The analysis reveals a notorious spatial variability and augmented values at the sloping topography ($\varepsilon \approx 5 \times 10^{-8}$ W kg^{-1}). For the 60 to 80 m depth range, dissipation estimates between interior and slope differ by 3 to 4 orders of magnitude. The enhanced turbulence adjacent to the sloping topography consistently localizes at depths above the known extent of bottom boundary layers in Lake Geneva (∼10 m; Bouffard & Lemmin, 2013a) and, in general, for medium (e.g., Wüest et al., 2000) and large lakes (Ravens et al., 2000; Troy et al., 2016). Therefore, another hydrodynamic process may have triggered this response.

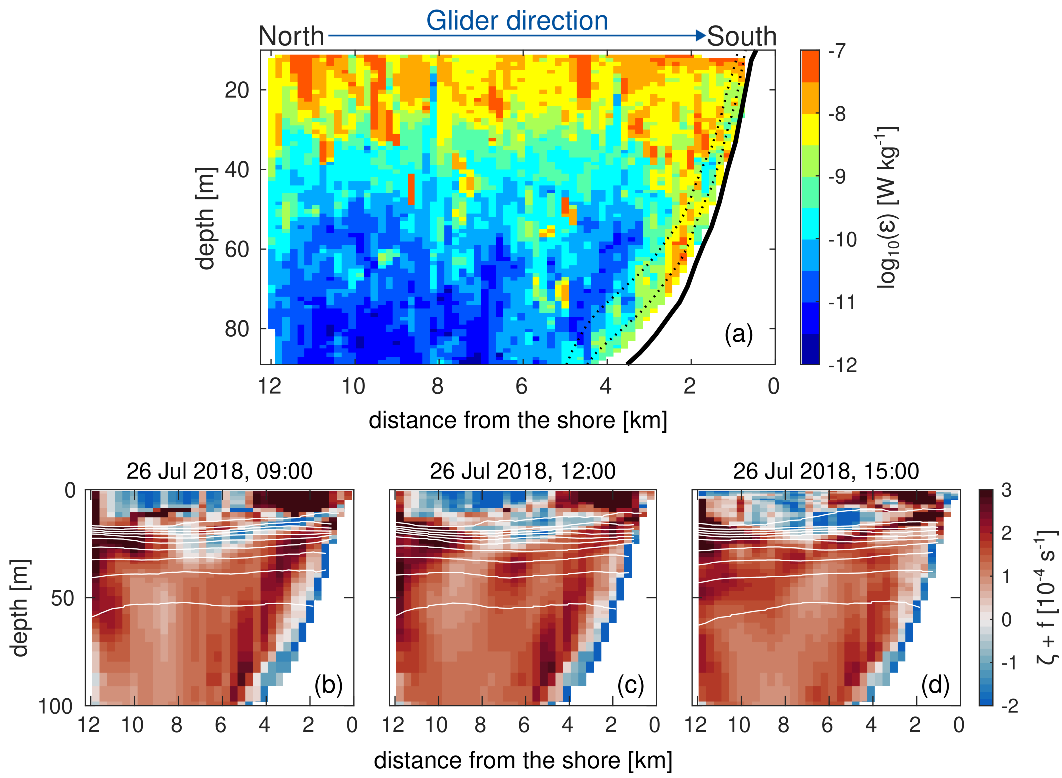

Figure 9. Cross-shore lateral variability. Data corresponding to mission M0, performed on 26 Jul 2018, starting at 10:50 am local time. (a) Glider-based turbulent dissipation (ε). The thick black line represents the lake bottom, with dotted black lines depicting the vertical displacements of the lake bed by 10 and 20 m, respectively. The collection of microstructure data was only possible due to the gentle slope of the mapped area. (b-d) Transects showing the sum of vertical relative vorticity, ζ, and the inertial frequency, f, as obtained from `meteolakes.ch` for different times of the same day. White lines in (b-d) correspond to temperature isolines.

4.5 Sources of variability

During the field campaign, wind measurements (Figure 10a) show moderate intensity, occasionally exceeding 5 m s^{-1}, and a predominant North-East direction (*La Bise*). Strong winds, consistently exceeding 5 m s^{-1}, were sporadic and associated with Le Vent events (South-West winds). Overall, the primary forcing was *La Bise* and exhibited a daily cycle (Figure 10b).

We complemented our glider measurements with observations of horizontal current profiles at four different locations to obtain background information on basin-scale processes, which drive spatial variability. Time series of current measurements from the four stations (Figure 2) are presented in Figure S12. Currents at the Buchillon coastal station (shallow waters) were more energetic than those measured in the interior, with dominant low-frequency periodicities (Figures 10b,c). In the lake interior, currents' rotary spectra (Figures 10b,c) were remarkably similar for the three open water monitored locations (ADCPs 1 to 3). Energized frequencies near the inertial frequency (period of ∼16.6 h for L. Geneva) in the clockwise component indicate the presence of Poincaré internal waves. This phenomenon has been identified to generate turbulent mixing in the lake interior (Bouffard et al., 2012). However, our results (Figure 8a-c) do not support that mechanism of mixing generation. At the Buchillon shore station, spectral energy levels at low frequencies exceed those of the interior. These peaks occur at the expected bands of basin-scale internal Kelvin waves (Bouffard & Lemmin, 2013a) and gyres.

Times series of band-pass filtered HKE at the near-inertial frequency (Figure 10d) were markedly variable during the glider missions. The level of energy contained in the near-inertial range was high during M3 but minimal during M1 and M5. Inertial currents radius (Figure 10d) was 0.2 to 0.4 km during the glider missions, which given our programmed flight mission (∼0.5 km between consecutive yo's), it is not optimal for detecting spatial variability.

5 Discussion

5.1 Glider deployments and their sampling potential in lakes

This study reports and evaluates spatiotemporal heterogeneities of turbulence in a large lake using an underwater glider. While mounting turbulence packages on gliders is now close to standard for oceanic measurements (e.g., Fer et al., 2014; Scheifele et al., 2018), such observations remain rare in lakes. Our results indicate that glider-based missions yield reliable turbulence measurements even in low turbulence and strongly stratified environments (Figures 5,6,7,S11) while collecting water quality parameters susceptible to turbulent transport (Figures S2-S7).

Gliders enable scanning lateral variability of water constituents and small-scale turbulence over long periods. Yet, the relevance of the data collected by glider missions depends on the spatial scale of interest. Our flight immersion until ∼100 m depth seriously altered the possibility of investigating fine horizontal structures at the thermocline, given the approximate 0.5 km horizontal distance between two consecutive dives. It is tempting to infer from the results that the interior's upper layer is relatively homogeneous and, therefore, a 1D representation would be sufficient (Figure 3). This interpretation could be a mistake because the dominant basin-scale process, namely near-inertial waves (Figure 10), may induce horizontal stirring at scales smaller than 0.5 km. From the ADCP measurements, we estimated the horizontal kinetic energy and the characteristic inertial radius resulting from current-induced circulation at the dominant inertial frequency band (Figure 10c). This characteristic length is in the range of 0.2 to 0.4 km, suggesting that the horizontal variability resulting from near-inertial waves is smaller than the scale characterized by our glider missions.

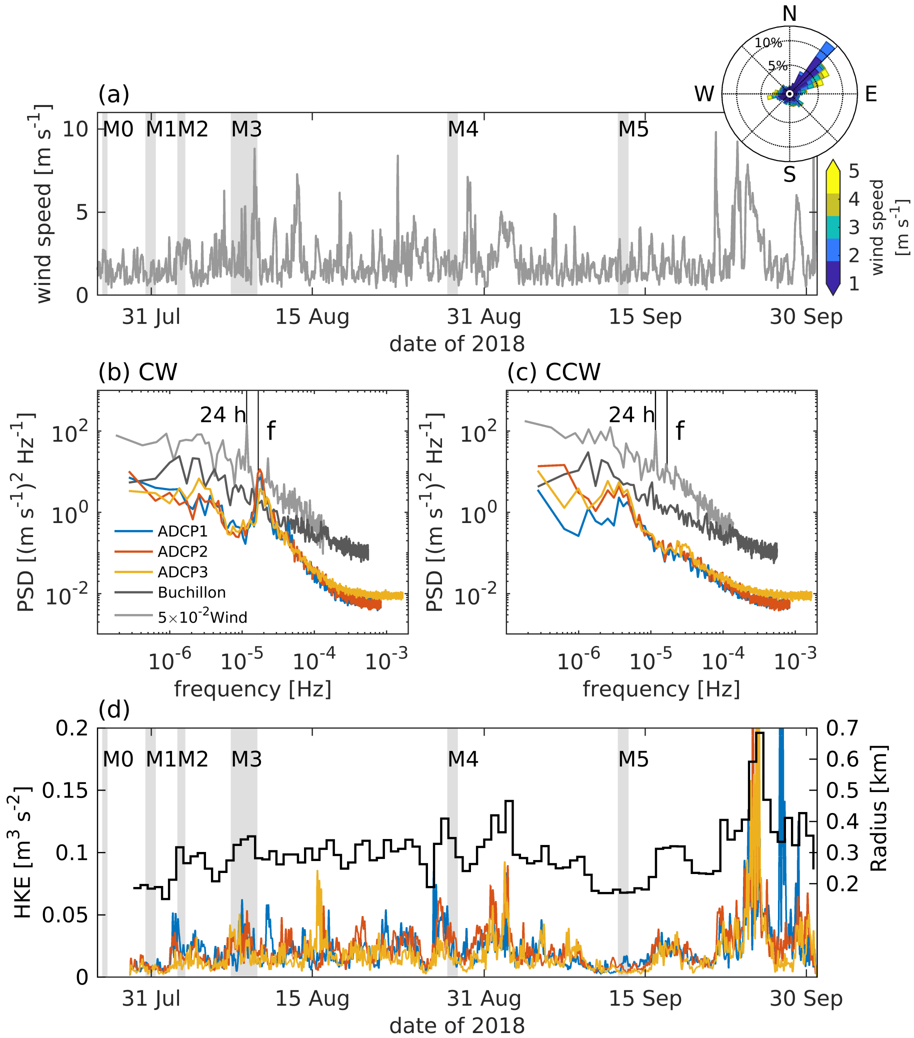

Figure 10. Wind data and current measurements analysis. (a) Wind speed time series and wind rose (direction) as measured at the Buchillon station. (b,c) Median rotary power spectral density (PSD) for clockwise (CW; anti-cyclonic in northern hemisphere) and counter-clockwise (CCW; cyclonic) current components, respectively. The analysis considers the currents time series for each sampled bin throughout the water column. For convenience, the wind rotary PSD is presented scaled by a factor of 5×10^{-2} to match the scale of currents PSDs. The inertial frequency is indicated by f and corresponds to a period of 16.6 h. (d) Left y-axis: Horizontal kinetic energy (HKE) of the inertial range of currents for ADCP1 to ADCP3. A bandpass filter around the inertial frequency of $[1, 5]\times10^{-5}$ Hz was applied to the currents to perform the calculations. Right y-axis: Median radius of inertial currents (black line) obtained from the three HKE estimates, filtered with a 16 h window average. Gray areas in (a) and (c) denote the periods of each glider mission.

Prior knowledge of the characteristic length scales of the investigated process is critical to evaluating whether or not gliders can provide meaningful information. Although our mission design pushed the capabilities of safe glider navigation to the limit, standard CTD transects can easily outcompete the spatial resolution gliders render by resigning temporal coverage. As it would take longer to complete the transect for each profile added. Gliders will perform at best when the enabled scanning resolves the length scales of the studied process. Therefore, targeting processes that exhibit characteristic length scales of several kilometers, such as gyres (Laval et al., 2005; Shimizu et al., 2007) and coastal upwelling events (Reiss et al., 2020; Roberts et al., 2021), would ensure good performance. Nevertheless, equipping gliders with shallow pumps to improve underwater sampling agility is a strategy that would allow increasing spatial resolution in the upper layers of medium and large lakes.

A significant and distinct advantage of glider-based missions is the possibility to collect data during traditionally challenging weather conditions (strong winds, severe sea states). In lakes, under such conditions, gliders enable measurements that would be otherwise impossible to obtain through ship-based operations. This challenge is particularly relevant for turbulent quantities, often requiring tethered, free-falling profilers that are likely to hit the bottom when the line drop is not vertical due to wind- or current-driven boat drift. Therefore, underwater gliders represent a qualitative breakthrough for data acquisition in large lakes.

5.2 Turbulence estimates

Glider-based turbulence measurements have been mainly documented for energetic ocean environments (Fer et al., 2014; Schultze et al., 2017). The weak-to-moderate energetics of the strongly stratified Lake Geneva contrasts with the common use of gliders for turbulence estimates in oceanic conditions. This work reports a comprehensive method validation because gliders' along-path speeds ($U \approx 0.35$ m s^{-1}; this research) are two times faster than usual microstructure profiling speeds for lakes ($U \approx 0.15$ m s^{-1}; Kocsis et al., 1999). We followed the approach of Dillon and Caldwell (1980), binned temperature microstructure spectra in different ranges of Cox number, and calculated their ensemble average (Figure 5). The analysis demonstrates that spectra meeting the Batchelor fitting conditions capture the variance and roll-off characteristics of the theoretical shape. Therefore, the procedure ensures reliable turbulence estimates that, as expected, were less energetic than in the ocean.

Turbulence estimates in the interior presented a marked vertical structure with maximal values close to the surface ($\sim 10^{-7}$ W kg^{-1}) that weakened with depth ($\sim 10^{-11}$ W kg^{-1}). This result is consistent with the interior vertical profile in other deep stratified lakes (Fernández Castro, Sepúlveda Steiner, et al., 2021; Ravens et al., 2000). For a cross-shore transect, the vertical decay of turbulent dissipation rates was more gradual and ranged between $10^{-10} - 10^{-8}$ W kg^{-1} in the deeper layers, which agrees with average summer profiles reported for Lake Geneva in a coastal location (Fernández Castro, Bouffard, et al., 2021).

5.3 Mixing characterization

This work provides spatially-distributed turbulent mixing estimates from a glider in a large lake. The interior thermocline region shows a combination of strong stratification and moderate TKE dissipation (Figure 7a). The strong background temperature gradient leads to reduced Cox numbers ($C_x < 1$), suggesting that there is no turbulent mixing, despite $Re_b > 7$ (i.e., transition to turbulence) in the water column (Figure 8a,c between 10 and 40 m). Our analysis revealed inhibited mixing in the thermocline ($Ri_f \sim 0.01$) and mixing efficiency below the canonical oceanic value in the deep interior ($Ri_f < Ri_f^{ocean} = 0.17$; Osborn, 1980). The extremely low mixing efficiency in the thermocline is in line with several studies using microstructure and other indirect methods (e.g., Wüest et al., 2000; Etemad-

Shahidi & Imberger, 2001) but differs from the strong thermocline dissipation observed by Bouffard and Boegman (2013) in the shallow and energetic Lake Erie.

In the coastal transition zone, mixing was active ($C_x > 1$, $Ri_f > 0.1$) below 20 m depth, even developing energetic turbulent regimes ($Re_b > 100$). This highlights the clear difference between interior and coastal slope regions in lakes and the role of boundary conditions in the generation of turbulent mixing (Gloor et al., 2000; Goudsmit et al., 1997).

There is a long-standing debate on whether assuming mixing efficiency as a constant ($Ri_f = 0.17$ in the ocean; Osborn, 1980) or parameterized as a function of turbulence characteristics. The constant viewpoint stems from the uncertainty level of observations, whereas several studies dealing with microstructure-based turbulent quantities propose various parameterizations (e.g., Ivey et al., 2008; Bouffard & Boegman, 2013; Monismith et al., 2018). The glider-based turbulence dataset, collected in the lake interior, allows us to analyze the sensitivity of Ri_f to different turbulent parameters, such as C_x and Re_b (Figure 11).

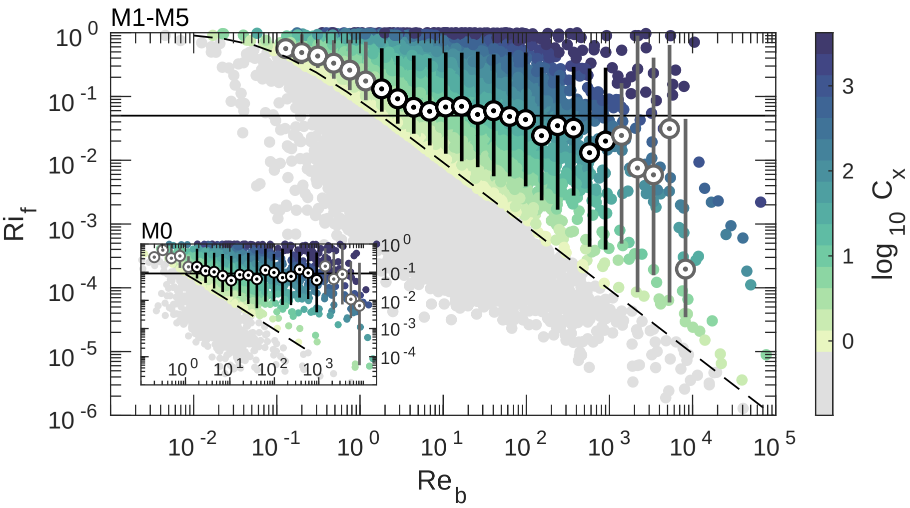

Figure 11. Mixing diagram. Richardson flux number (Ri_f) as a function of the buoyancy Reynolds number (Re_b) and color-coded for Cox numbers (C_x) for the lake interior data set (M1-M5). Dotted white circles represent the median of Ri_f in each bin for data points with $C_x > 1$. Error bars show 10th and 90th percentiles of the same subset. Black dotted-circles represent statistically well-conditioned intervals, with a reliable amount of data points, whereas those in gray are irrelevant or less reliable due to $Re \leq 1$ or few data points ($Re > 10^3$ intervals). The dashed black line is Ri_f expressed as a function of C_x and Re_b, $Ri_f(C_x, Re_b) = \frac{C_x(D_T/\nu)}{C_x(D_T/\nu)+Re_b}$ for $C_x = 1$. The horizontal black line corresponds to the median of the statistically well-conditioned interval $Ri_f = 0.05$. The inset plot in the left-inferior corner depicts the same analysis for the interior-to-coast transition data set (M0), with a median of $Ri_f = 0.09$.

For the interior, the comparison of Ri_f as a function of Re_b (Figure 11) shows a large scatter with values spanning more than five decades. Binning data points with $C_x > 1$ only (i.e., turbulent temperature fluctuations overcome the background gradient) and averaging within the domain $1 < Re_b < 1000$ yields $Ri_f \approx 0.05$. For a compilation of oceanic datasets, Monismith et al. (2018) found $Ri_f \approx 0.17$ when considering data from below the thermocline. The same analysis for the cross-shore transect data (M0; inset in Figure 11) indicates $Ri_f \approx 0.09$, only slightly more efficient than the interior despite the considerable enhancement of turbulence close to the sloping boundary (Figure 9a). Altogether, Figure 11 reveals that turbulent mixing in Lake Geneva was considerably less efficient during our sampling than in the ocean, raising concerns about the applicability of the Osborn diffusivity model in lakes. Therefore, mixing efficiency in deep, strongly stratified, and weakly energized lakes requires further research. Notwithstanding, Figure 11 clearly shows the dependency of Ri_f on C_x and Re_b, supporting the need for more elaborated parameterizations of mixing efficiency (e.g., Mashayek et al., 2021).

5.4 Lateral variability of turbulence along sloping topography

The transect towards the southern shore of Lake Geneva (Figure 9a) captured considerable horizontal variability of turbulent dissipation. An intuitive and plausible process generating such a feature is internal wave breaking (Lorke, 2007; Nakayama et al., 2020), but we do not have temporally resolved temperature profile data to assess it. Comparable measurements in Lake Geneva were performed with microstructure sensors mounted on a piloted submarine (Fer et al., 2002). Although their measurements correspond to winter, when stratification is weaker, our turbulent dissipation estimates near the slopes ($10^{-9} - 10^{-7}$ W kg^{-1}; Figure 9a) agree with those of Fer et al. (2002), reported for windy conditions. Our measurements reveal a more intense mixing at the boundaries, supporting results from tracer release experiments (e.g., Goudsmit et al., 1997) and microstructure studies (e.g., Bouffard et al., 2012). For unknown reasons, the high dissipation rates observed in the coastal region during mission M0 extended 10 to 20 m above the expected bottom boundary layer ($\sim$10 m thickness in L. Geneva; Bouffard & Lemmin, 2013a).

During our measurements, the interior of Lake Geneva resulted in a challenging environment for the assessment of horizontal variability due to a lack of prominent hydrodynamic features. However, Figure 9a suggests that glider deployments could be valuable to study cross-shore turbulence patterns, particularly when approaching sloping boundaries. Safe glider navigation through steep bathymetry is the main complication to advance this knowledge. A more agile underwater glider (i.e., equipped with a shallow pump enabling faster vertical turns) and interactive navigation strategies interfacing glider-mounted acoustics could help overcome this technical barrier.

5.5 Centrifugal instabilities

Recent advancements in ocean research have identified centrifugal instabilities as a mechanism transferring kinetic rotational energy from geostrophic flows to the submesoscales and, subsequently, to small-scale turbulence (Gula et al., 2016). These instabilities alter circulation driving unbalanced motions, and promote horizontal transport. Specifically, centrifugal instabilities caused by interactions between cyclonic currents (counter-clockwise in the northern hemisphere) and the sloping bathymetry can trigger vigorous turbulent mixing (Naveira Garabato et al., 2019; Wenegrat & Thomas, 2020). We hypothesize that this mechanism may account for the enhanced turbulence adjacent to the sloping topography above the expected bottom boundary layer in our cross-shore transect (Figure 9a).

The occurrence of these instabilities is tied to the direction of the vertical component of Ertel's potential vorticity, q_v, by:

$$q_v = (\zeta + f)N^2 < 0 \tag{9}$$

where $\zeta = \frac{\partial v}{\partial x} - \frac{\partial u}{\partial y}$ is the vertical relative vorticity with u and v the east- and north-ward velocity component, respectively and f the inertial frequency. In simple words, centrifugal instabilities develop in the presence of cyclonic background circulation (e.g., a Kelvin wave) when the resulting vertical relative vorticity is negative, and its magnitude exceeds the Earth rotational forcing.

We used velocity results from the open-access lake forecast model `meteolakes.ch` (Baracchini et al., 2020) to extract the vertical relative vorticity and evaluate our hypothesis. Figure S13 offers validation of the model results. The resemblance of model velocities' rotary spectra (Figure S13i,j) at the different ADCP stations (Figure 2) indicates that the model can resolve the main basin-scale processes. We acknowledge the coarse resolution of the available model (450 m horizontal grid) and recognize that a dedicated finer resolution model would better resolve the velocity field. However, even from the horizontal resolution used in `meteolakes.ch` (>10 grid points in one Rossby radius), it is possible to evaluate the potential for the occurrence of centrifugal instabilities. Figures 9b-c show $\zeta + f$ at three times during the same day of M0 along the glider's transect. On the sloping topography section, $\zeta + f < 0$, signaling the presence of unstable flow 20 m above the bottom. This first approach confirms the potential for centrifugal instabilities.

Notably, the cyclonic current exceeding the inertial effect (e.g., Figures 9b-c) seems to last for approximately one inertial period (16.6 h; $f = 1.05 \times 10^{-4}$ s^{-1}), which sets the minimal time-scale required for the development of centrifugal instabilities. Hence, the flow interaction with the sloping topography could unfold centrifugal instabilities and would explain the elevated turbulent dissipation encountered around 19:00 h during M0 (Figure 9a). Further comparison of geometrical and hydrodynamic characteristics can inform on the likelihood of instabilities occurrence by comparing the gradient Richardson number (Ri_g) with the slope Burger number (Wenegrat et al., 2018). The former is canonical ($Ri_g = N^2/S^2$, where $S^2 = (\partial u/\partial z)^2 + (\partial v/\partial z)^2$ is the vertical shear squared) while the slope Burger number is defined by:

$$S_{Bu} = \left(\frac{\beta N}{f}\right)^2 \tag{10}$$

where β (m m^{-1}) is the bathymetric slope. Numerical analyses by Wenegrat et al. (2018) indicate that centrifugal instabilities will develop at sloping bottoms when $S_{Bu} > Ri_g$ for S_{Bu}, $Ri_g \geq 1$. The region scanned by the glider during M0 exhibits $\beta \approx 0.030$; thus, $S_{Bu} \geq 1$ for $N^2 \geq 1.25 \times 10^{-5}$ s^{-2}, which is largely fulfilled for our measurements. Yet, `meteolakes.ch` results indicate $S^2 \approx 10^{-5}$ s^{-2} at the slope, which renders $S_{Bu} \sim Ri_g$. Therefore, according to Wenegrat et al. (2018), the conditions during M0 could trigger centrifugal instabilities, although the analysis is not categorical.

Centrifugal instabilities have been identified as crucial mechanisms for energy cascading and mixing at slopes in the Gulf Stream (Gula et al., 2016) and deep boundary currents (Naveira Garabato et al., 2019). However, in lakes, this process remains overlooked. The coastal region of lakes develops recurrent cyclonic motions such as Kelvin waves, coastal jets, and gyres. Therefore, as defined by Wenegrat et al. (2018), this process is likely to occur on gentle slopes during stratified conditions. As closing energy budgets in lakes remains elusive, further investigations of centrifugal instabilities may reveal unaccounted transport and mixing processes key to expanding these budgets to the spatial extent. Combining a cross-shore array of high vertical resolution moorings resolving temperature (e.g., van Haren, 2018; van Haren et al., 2021) and velocity fluctuations with repeated glider transects could be an interesting strategy for future exploration.

6 Conclusions

Our glider-based observations and analyses of spatially-distributed water physical quantities in Lake Geneva offer the following conclusions:

1. We present the first comprehensive study of underwater glider-based turbulence measurements in lakes. Moreover, we validate the use of such moving platforms for turbulent dissipation estimates using temperature microstructure despite the strong stratification and weak-to-moderate energetics.

2. Our results indicate that gliders are better suited for characterizing spatial variability when focusing on basin-scale processes with characteristic scales larger than the resolution enabled by two consecutive profiles (or yo's). However, despite the specific conditions during the sampling in Lake Geneva, we provide a compelling example of how they enable connecting large to small (turbulence) scales and vertical to horizontal dimensions.

3. Despite the comparatively elevated turbulent dissipation, consistent with the level of wind forcing, our study strongly suggests that the thermocline region exhibited inhibited mixing due to the strong stratification.

4. We observed an increase in water column dissipation near the lake coastal slope and suggest that centrifugal instabilities, a previously unaccounted process in lakes, could explain the enhanced near-boundary turbulence observations. Cyclonic circulation perpendicular to the gentle sampled slope forced this process. As these flow conditions are ubiquitous in large lakes (e.g., basin-scale internal Kelvin waves and gyres), centrifugal instabilities are a potentially critical mechanism to study in other similar lakes.

Much effort is still needed to unravel the spatial extent of energy budgets in lakes. This research provides a first step towards that direction. Future research could combine the approach presented here with seasonal monitoring of turbulence microstructure and small-scale velocity field in bottom boundary layers (Fernández Castro, Bouffard, et al., 2021) to reveal temporal and lake-wide resolved energy pathways.

Data Availability Statement

Field measurements (glider and ADCPs) supporting the findings of this research are available online (`zenodo-link-to-be-created`). Meteorological data is available at `https://www.datalakes-eawag.ch` Data Portal (Buchillon Field Station). Lake Geneva 3D model results are available at `www.meteolakes.ch` (Data Order/API).

Acknowledgments

We want to thank Hannah Chmiel, Theo Baracchini, Rafael Reiss, and Claudio Thomas Halaby for their assistance during fieldwork and Cordielyn Goodrich for remote surveillance of the glider during overnight missions. Anton Schleiss kindly allowed us to use his pool for ballasting purposes. The staff of Rockland Scientific provided timely feedback and troubleshooting during the field campaign.

We are grateful to Lucas Merckelbach for guidance and technical support with the flight model and Ilker Fer and Andreas Lorke for their comments on an early version of the manuscript. Valuable feedback from Alberto Naveira Garabato on centrifugal instabilities, Cintia Ramón Casañas on numerical simulations and Jay Austin on rotary spectra helped improve the manuscript's presentation and discussion.

We acknowledge Theo Baracchini for leading the development of `meteolakes.ch` and James Runnalls for currently maintaining it.

Funding

This work was funded by the Swiss National Science Foundation Sinergia grant CRSII2_160726 (*A Flexible Underwater Distributed Robotic System for High-Resolution Sensing of Aquatic Ecosystems*). The ENAC Visiting Professor Program funded A.L.F's visit to EPFL during 2018.

References

Adrian, R., O'Reilly, C. M., Zagarese, H., Baines, S. B., Hessen, D. O., Keller, W., ... Winder, M. (2009). Lakes as sentinels of climate change. *Limnology and Oceanography*, *54*(6part2), 2283-2297. doi: https://doi.org/10.4319/lo.2009.54.6_part_2.2283

Alexander, R., & Imberger, J. (2013). Phytoplankton patchiness in Winam Gulf, Lake Victoria: a study using principal component analysis of in situ fluorescent excitation spectra. *Freshwater Biology*, *58*(2), 275–291. doi: https://doi.org/10.1111/fwb.12057

Antenucci, J. P., Imberger, J., & Saggio, A. (2000). Seasonal evolution of the basin-scale internal wave field in a large stratified lake. *Limnology and Oceanography*, *45*(7), 1621–1638. doi: https://doi.org/10.4319/lo.2000.45.7.1621

Appt, J., Imberger, J., & Kobus, H. (2004). Basin-scale motion in stratified Upper Lake Constance. *Limnology and Oceanography*, *49*(4), 919–933. doi: https://doi.org/10.4319/lo.2004.49.4.0919

Austin, J. (2012). Resolving a persistent offshore surface temperature maximum in Lake Superior using an autonomous underwater glider. *Aquatic Ecosystem Health and Management*, *15*(3), 316–321. doi: https://doi.org/10.1080/14634988.2012.711212

Austin, J. (2013). The potential for autonomous underwater gliders in large lake research. *Journal of Great Lakes Research*, *39*(S1), 8–13. doi: https://doi.org/10.1016/j.jglr.2013.01.004

Austin, J. (2019). Observations of radiatively driven convection in a deep lake. *Limnology and Oceanography*, *64*(5), 2152–2160. doi: https://doi.org/10.1002/lno.11175

Baker, M. A., & Gibson, C. H. (1987). Sampling turbulence in the stratified ocean: Statistical consequences of strong intermittency. *Journal of Physical Oceanography*, *17*(10), 1817–1836. doi: https://doi.org/10.1175/1520-0485(1987)017⟨1817:STITSO⟩2.0.CO;2

Baracchini, T., Wüest, A., & Bouffard, D. (2020). Meteolakes: An operational online three-dimensional forecasting platform for lake hydrodynamics. *Water Research*, *172*, 115529. doi: https://doi.org/10.1016/j.watres.2020.115529

Batchelor, G. K. (1959). Small-scale variation of convected quantities like temperature in turbulent fluid Part 1. General discussion and the case of small conductivity. *Journal of Fluid Mechanics*, *5*(1), 113–133. doi: https://doi.org/10.1017/S002211205900009X

Bauer, S. W., Graf, W. H., Mortimer, C. H., & Perrinjaquet, C. (1981). Inertial motion in Lake Geneva (Le Léman). *Archives for Meteorology, Geophysics, and Bioclimatology Series A*, *30*(3), 289–312. doi: https://doi.org/10.1007/BF02257850

Bohle-Carbonell, M. (1986). Currents in Lake Geneva. *Limnology and Oceanography*, *31*(6), 1255–1266. doi: https://doi.org/10.4319/lo.1986.31.6.1255

Bouffard, D., & Boegman, L. (2013). A diapycnal diffusivity model for stratified environmental flows. *Dynamics of Atmospheres and Oceans*, *61-62*, 14–34. doi: https://doi.org/10.1016/j.dynatmoce.2013.02.002

Bouffard, D., Boegman, L., & Rao, Y. R. (2012). Poincaré wave–induced mixing in a large lake. *Limnology and Oceanography*, *57*(4), 1201–1216. doi: https://doi.org/10.4319/lo.2012.57.4.1201

Bouffard, D., & Lemmin, U. (2013a). Kelvin waves in Lake Geneva. *Journal of Great Lakes Research*, *39*(4), 637–645. doi: https://doi.org/10.1016/j.jglr.2013.09.005

Bouffard, D., & Lemmin, U. (2013b). A new sensor platform for investigating turbulence in stratified coastal environments. *Journal of Atmospheric and Oceanic Technology*, *30*(8), 1789–1802. doi: https://doi.org/10.1175/JTECH-D-12-00159.1

Csanady, G. T. (1975). Hydrodynamics of large lakes. *Annual Review of Fluid Mechanics*, *7*(1), 357–386. doi: https://doi.org/10.1146/annurev.fl.07.010175.002041

Davis, R. E., Eriksen, C. C., & Jones, C. (2002). Autonomous buoyancy-driven underwater gliders. In G. Griffiths (Ed.), *Technology and applications of autonomous underwater vehicles* (pp. 37–58). Taylor & Francis. doi: https://doi.org/10.1201/9780203522301.ch3

Dillon, T. M., & Caldwell, D. R. (1980). The Batchelor spectrum and dissipation in the upper ocean. *Journal of Geophysical Research*, *85*(C4), 1910–1916. doi: https://

doi.org/10.1029/JC085iC04p01910
Etemad-Shahidi, A., & Imberger, J. (2001). Anatomy of turbulence in thermally stratified lakes. *Limnology and Oceanography*, *46*(5), 1158–1170. doi: https://doi.org/10.4319/lo.2001.46.5.1158
Fer, I., Lemmin, U., & Thorpe, S. A. (2002). Observations of mixing near the sides of a deep lake in winter. *Limnology and Oceanography*, *47*(2), 535–544. doi: https://doi.org/10.4319/lo.2002.47.2.0535
Fer, I., Peterson, A. K., & Ullgren, J. E. (2014). Microstructure measurements from an underwater glider in the turbulent Faroe Bank Channel overflow. *Journal of Atmospheric and Oceanic Technology*, *31*(5), 1128–1150. doi: https://doi.org/10.1175/JTECH-D-13-00221.1
Fernández Castro, B., Bouffard, D., Troy, C., Ulloa, H. N., Piccolroaz, S., Sepúlveda Steiner, O., ... Wüest, A. (2021). Seasonality modulates wind-driven mixing pathways in a large lake. *Communications Earth & Environment*, *2*(1), 215. doi: https://doi.org/10.1038/s43247-021-00288-3
Fernández Castro, B., Sepúlveda Steiner, O., Knapp, D., Posch, T., Bouffard, D., & Wüest, A. (2021). Inhibited vertical mixing and seasonal persistence of a thin cyanobacterial layer in a stratified lake. *Aquatic Sciences*, *83*(2), 38. doi: https://doi.org/10.1007/s00027-021-00785-9
Forrest, A. L., Laval, B. E., Pieters, R., & Lim, D. S. S. (2008). Convectively driven transport in temperate lakes. *Limnology and Oceanography*, *53*(5), 2321–2332. doi: https://doi.org/10.4319/lo.2008.53.5_part_2.2321
Frajka-Williams, E., Eriksen, C. C., Rhines, P. B., & Harcourt, R. R. (2011). Determining vertical water velocities from Seaglider. *Journal of Atmospheric and Oceanic Technology*, *28*(12), 1641–1656. doi: https://doi.org/10.1175/2011JTECHO830.1
Gargett, A. E., Osborn, T. R., & Nasmyth, P. W. (1984). Local isotropy and the decay of turbulence in a stratified fluid. *Journal of Fluid Mechanics*, *144*, 231–280. doi: https://doi.org/10.1017/S0022112084001592
Gibson, C. H. (1980). Fossil temperature, salinity, and vorticity turbulence in the ocean. In J. C. Nihoul (Ed.), *Marine turbulence proceedings of the 11th International Liege colloquium on ocean hydrodynamics, Elsevier Oceanography Series* (Vol. 28, pp. 221–257). New York NY: Elsevier/North-Holland Inc. doi: https://doi.org/10.1016/S0422-9894(08)71223-6
Gloor, M., Wüest, A., & Imboden, D. M. (2000). Dynamics of mixed bottom boundary layers and its implications for diapycnal transport in a stratified, natural water basin. *Journal of Geophysical Research: Oceans*, *105*(C4), 8629–8646. doi: https://doi.org/10.1029/1999JC900303
Goudsmit, G.-H., Peeters, F., Gloor, M., & Wüest, A. (1997). Boundary versus internal diapycnal mixing in stratified natural waters. *Journal of Geophysical Research*, *102*(C13), 27903–27914. doi: https://doi.org/10.1029/97JC01861
Gregg, M. C. (1977). Variations in the intensity of small-scale mixing in the main thermocline. *Journal of Physical Oceanography*, *7*, 436–454. doi: https://doi.org/10.1175/1520-0485(1977)007⟨0436:VITIOS⟩2.0.CO;2
Gula, J., Molemaker, M. J., & McWilliams, J. C. (2016). Topographic generation of submesoscale centrifugal instability and energy dissipation. *Nature Communications*, *7*, 12811. doi: https://doi.org/10.1038/ncomms12811
Imberger, J. (1998). Flux paths in a stratified lake: A review. In J. Imberger (Ed.), *Physical processes in lakes and oceans* (p. 1-17). American Geophysical Union (AGU). doi: https://doi.org/10.1029/CE054p0001
Imberger, J., & Ivey, G. N. (1991). On the nature of turbulence in a stratified fluid. Part II: Application to lakes. *Journal of Physical Oceanography*, *21*(5), 659–680. doi: https://doi.org/10.1175/1520-0485(1991)021⟨0659:OTNOTI⟩2.0.CO;2
Ishikawa, K., Kumagai, M., Vincent, W. F., Tsujimura, S., & Nakahara, H. (2002). Transport and accumulation of bloom-forming cyanobacteria in a large, mid-latitude lake: The gyre-Microcystis hypothesis. *Limnology*, *3*(2), 87–96. doi: https://doi.org/

10.1007/s102010200010
Ivey, G. N., & Imberger, J. (1991). On the nature of turbulence in a stratified fluid. Part I: The energetics of mixing. *Journal of Physical Oceanography*, *21*(5), 650–658. doi: https://doi.org/10.1175/1520-0485(1991)021⟨0650:OTNOTI⟩2.0.CO;2
Ivey, G. N., Winters, K. B., & Koseff, J. R. (2008). Density stratification, turbulence, but how much mixing? *Annual Review of Fluid Mechanics*, *40*(1), 169–184. doi: https://doi.org/10.1146/annurev.fluid.39.050905.110314
Jassby, A., & Powell, T. (1975). Vertical patterns of eddy diffusion during stratification in Castle Lake, California. *Limnology and Oceanography*, *20*(4), 530-543. doi: https://doi.org/10.4319/lo.1975.20.4.0530
Kocsis, O., Prandke, H., Stips, A., Simon, A., & Wüest, A. (1999). Comparison of dissipation of turbulent kinetic energy determined from shear and temperature microstructure. *Journal of Marine Systems*, *21*(1-4), 67–84. doi: https://doi.org/10.1016/S0924-7963(99)00006-8
Laval, B., Bird, J. S., & Helland, P. D. (2000). An autonomous underwater vehicle for the study of small lakes. *Journal of Atmospheric and Oceanic Technology*, *17*(1), 69–76. doi: https://doi.org/10.1175/1520-0426(2000)017⟨0069:AAUVFT⟩2.0.CO;2
Laval, B., Imberger, J., & Findikakis, A. N. (2005). Dynamics of a large tropical lake: Lake Maracaibo. *Aquatic Sciences*, *67*(3), 337–349. doi: https://doi.org/10.1007/s00027-005-0778-1
Lemckert, C., Antenucci, J., Saggio, A., & Imberger, J. (2004). Physical properties of turbulent benthic boundary layers generated by internal waves. *Journal of Hydraulic Engineering*, *130*(1), 58–69. doi: https://doi.org/10.1061/(ASCE)0733-9429(2004)130:1(58)
Lemmin, U., & D'Adamo, N. (1996). Summertime winds and direct cyclonic circulation: observations from Lake Geneva. *Annales Geophysicae*, *14*(11), 1207–1220. doi: https://doi.org/10.1007/s00585-996-1207-z
Lemmin, U., Mortimer, C. H., & Bäuerle, E. (2005). Internal seiche dynamics in Lake Geneva. *Limnology and Oceanography*, *50*(1), 207–216. doi: https://doi.org/10.4319/lo.2005.50.1.0207
Lorke, A. (2007). Boundary mixing in the thermocline of a large lake. *Journal of Geophysical Research: Oceans*, *112*, C09019. doi: https://doi.org/10.1029/2006JC004008
Lucas, N. S., Grant, A. L. M., Rippeth, T. P., Polton, J. A., Palmer, M. R., Brannigan, L., & Belcher, S. E. (2019). Evolution of oceanic near-surface stratification in response to an autumn storm. *Journal of Physical Oceanography*, *49*(11), 2961–2978. doi: https://doi.org/10.1175/JPO-D-19-0007.1
Luketina, D. A., & Imberger, J. (2001). Determining turbulent kinetic energy dissipation from Batchelor curve fitting. *Journal of Atmospheric and Oceanic Technology*, *18*(1), 100–113. doi: https://doi.org/10.1175/1520-0426(2001)018⟨0100:DTKEDF⟩2.0.CO;2
MacIntyre, S., Romero, J. R., & Kling, G. W. (2002). Spatial-temporal variability in surface layer deepening and lateral advection in an embayment of Lake Victoria, East Africa. *Limnology and Oceanography*, *47*(3), 656–671. doi: https://doi.org/10.4319/lo.2002.47.3.0656
MacIntyre, S., Romero, J. R., Silsbe, G. M., & Emery, B. M. (2014). Stratification and horizontal exchange in Lake Victoria, East Africa. *Limnology and Oceanography*, *59*(6), 1805–1838. doi: https://doi.org/10.4319/lo.2014.59.6.1805
Mashayek, A., Caulfield, C., & Alford, M. (2021). Goldilocks mixing in oceanic shear-induced turbulent overturns. *Journal of Fluid Mechanics*, *928*, A1. doi: 10.1017/jfm.2021.740
McDougall, T. J., & Barker, P. (2011). Getting started with TEOS-10 and the Gibbs Seawater (GSW) oceanographic toolbox. *SCOR/IAPSO WG.*, *127*, 1–28.
McInerney, J. B., Forrest, A. L., Schladow, S. G., & Largier, J. L. (2019). How to fly an autonomous underwater glider to measure an internal wave. In *OCEANS 2019 MTS/IEEE SEATTLE* (p. 1-8). doi: https://doi.org/10.23919/OCEANS40490.2019.8962407

Merckelbach, L., Berger, A., Krahmann, G., Dengler, M., & Carpenter, J. R. (2019). A dynamic flight model for Slocum gliders and implications for turbulence microstructure measurements. *Journal of Atmospheric and Oceanic Technology*, *36*(2), 281–296. doi: https://doi.org/10.1175/JTECH-D-18-0168.1

Merckelbach, L., Smeed, D., & Griffiths, G. (2010). Vertical water velocities from underwater gliders. *Journal of Atmospheric and Oceanic Technology*, *27*(3), 547–563. doi: https://doi.org/10.1175/2009JTECHO710.1

Michalski, J., & Lemmin, U. (1995). Dynamics of vertical mixing in the hypolimnion of a deep lake: Lake Geneva. *Limnology and Oceanography*, *40*(4), 809-816. doi: https://doi.org/10.4319/lo.1995.40.4.0809

Monismith, S. G., Koseff, J. R., & White, B. L. (2018). Mixing efficiency in the presence of stratification: When is it constant? *Geophysical Research Letters*, *45*(11), 5627–5634. doi: https://doi.org/10.1029/2018GL077229

Nakayama, K., Sato, T., Tani, K., Boegman, L., Fujita, I., & Shintani, T. (2020). Breaking of internal kelvin waves shoaling on a slope. *Journal of Geophysical Research: Oceans*, *125*(10), e2020JC016120. doi: https://doi.org/10.1029/2020JC016120

Naveira Garabato, A. C., Frajka-Williams, E. E., Spingys, C. P., Legg, S., Polzin, K. L., Forryan, A., ... Meredith, M. P. (2019). Rapid mixing and exchange of deep-ocean waters in an abyssal boundary current. *Proceedings of the National Academy of Sciences*, *116*(27), 13233–13238. doi: https://doi.org/10.1073/pnas.1904087116

Osborn, T. R. (1980). Estimates of the local rate of vertical diffusion from dissipation measurements. *Journal of Physical Oceanography*, *10*(1), 83–89. doi: https://doi.org/10.1175/1520-0485(1980)010⟨0083:EOTLRO⟩2.0.CO;2

Osborn, T. R., & Cox, C. S. (1972). Oceanic fine structure. *Geophysical Fluid Dynamics*, *3*(1), 321–345. doi: https://doi.org/10.1080/03091927208236085

Osborn, T. R., & Lueck, R. G. (1985). Turbulence measurements with a submarine. *Journal of Physical Oceanography*, *15*(11), 1502–1520. doi: https://doi.org/10.1175/1520-0485(1985)015⟨1502:TMWAS⟩2.0.CO;2

Peterson, A. K., & Fer, I. (2014). Dissipation measurements using temperature microstructure from an underwater glider. *Methods in Oceanography*, *10*, 44–69. doi: https://doi.org/10.1016/j.mio.2014.05.002

Ravens, T. M., Kocsis, O., Wüest, A., & Granin, N. (2000). Small-scale turbulence and vertical mixing in Lake Baikal. *Limnology and Oceanography*, *45*(1), 159–173. doi: https://doi.org/10.4319/lo.2000.45.1.0159

Reiss, R. S., Lemmin, U., Cimatoribus, A. A., & Barry, D. A. (2020). Wintertime coastal upwelling in Lake Geneva: An efficient transport process for deepwater renewal in a large, deep lake. *Journal of Geophysical Research: Oceans*, *125*(8), e2020JC016095. doi: https://doi.org/10.1029/2020JC016095

Roberts, D. C., Egan, G. C., Forrest, A. L., Largier, J. L., Bombardelli, F. A., Laval, B. E., ... Schladow, G. (2021). The setup and relaxation of spring upwelling in a deep, rotationally influenced lake. *Limnology and Oceanography*, *66*(4), 1168-1189. doi: https://doi.org/10.1002/lno.11673

Ruddick, B., Anis, A., & Thompson, K. (2000). Maximum likelihood spectral fitting: The Batchelor spectrum. *Journal of Atmospheric and Oceanic Technology*, *17*(11), 1541–1555. doi: https://doi.org/10.1175/1520-0426(2000)017⟨1541:MLSFTB⟩2.0.CO;2

Rudnick, D. L. (2016). Ocean research enabled by underwater gliders. *Annual Review of Marine Science*, *8*(1), 519–541. doi: https://doi.org/10.1146/annurev-marine-122414-033913

Saggio, A., & Imberger, J. (2001). Mixing and turbulent fluxes in the metalimnion of a stratified lake. *Limnology and Oceanography*, *46*(2), 392–409. doi: https://doi.org/10.4319/lo.2001.46.2.0392

Sahoo, G. B., Forrest, A. L., Schladow, S. G., Reuter, J. E., Coats, R., & Dettinger, M. (2016). Climate change impacts on lake thermal dynamics and ecosystem vulnerabilities. *Limnology and Oceanography*, *61*(2), 496-507. doi: https://doi.org/10.1002/lno.10228

Scheifele, B., Waterman, S., Merckelbach, L., & Carpenter, J. R. (2018). Measuring the dissipation rate of turbulent kinetic energy in strongly stratified, low-energy environments: A case study from the Arctic Ocean. *Journal of Geophysical Research: Oceans*, *123*(8), 5459–5480. doi: https://doi.org/10.1029/2017JC013731

Schladow, S. G., Pálmarsson, S. Ó., Steissberg, T. E., Hook, S. J., & Prata, F. E. (2004). An extraordinary upwelling event in a deep thermally stratified lake. *Geophysical Research Letters*, *31*(15), L15504. doi: https://doi.org/10.1029/2004GL020392

Schultze, L. K. P., Merckelbach, L. M., & Carpenter, J. R. (2017). Turbulence and mixing in a shallow shelf sea from underwater gliders. *Journal of Geophysical Research: Oceans*, *122*(11), 9092–9109. doi: https://doi.org/10.1002/2017JC012872

Schwefel, R., Gaudard, A., Wüest, A., & Bouffard, D. (2016). Effects of climate change on deepwater oxygen and winter mixing in a deep lake (Lake Geneva): Comparing observational findings and modeling. *Water Resources Research*, *52*(11), 8811–8826. doi: https://doi.org/10.1002/2016WR019194

Shimizu, K., Imberger, J., & Kumagai, M. (2007). Horizontal structure and excitation of primary motions in a strongly stratified lake. *Limnology and Oceanography*, *52*(6), 2641–2655. doi: https://doi.org/10.4319/lo.2007.52.6.2641

Sommer, T., Carpenter, J. R., Schmid, M., Lueck, R. G., & Wüest, A. (2013). Revisiting microstructure sensor responses with implications for double-diffusive fluxes. *Journal of Atmospheric and Oceanic Technology*, *30*(8), 1907–1923. doi: https://doi.org/10.1175/JTECH-D-12-00272.1

Steinbuck, J. V., Stacey, M. T., & Monismith, S. G. (2009). An evaluation of χ_T estimation techniques: Implications for Batchelor fitting and ε. *Journal of Atmospheric and Oceanic Technology*, *26*(8), 1652–1662. doi: https://doi.org/10.1175/2009JTECHO611.1

Thorpe, S. A. (2007). *An introduction to ocean turbulence.* Cambridge University Press. doi: https://doi.org/10.1017/CBO9780511801198

Thorpe, S. A., Lemmin, U., Perrinjaquet, C., & Fer, I. (1999). Observations of the thermal structure of a lake using a submarine. *Limnology and Oceanography*, *44*(6), 1575–1582. doi: https://doi.org/10.4319/lo.1999.44.6.1575

Troy, C., Cannon, D., Liao, Q., & Bootsma, H. (2016). Logarithmic velocity structure in the deep hypolimnetic waters of Lake Michigan. *Journal of Geophysical Research: Oceans*, *121*(1), 949–965. doi: https://doi.org/10.1002/2014JC010506

van Haren, H. (2018). Philosophy and application of high-resolution temperature sensors for stratified waters. *Sensors*, *18*(10), 3184. doi: https://doi.org/10.3390/s18103184

van Haren, H., Piccolroaz, S., Amadori, M., Toffolon, M., & Dijkstra, H. A. (2021). Moored observations of turbulent mixing events in deep Lake Garda, Italy. *Journal of Limnology*, *80*(1), 1983. doi: https://doi.org/10.4081/jlimnol.2020.1983

Webb, D. C., Simonetti, P. J., & Jones, C. P. (2001). Slocum: An underwater glider propelled by environmental energy. *IEEE Journal of Oceanic Engineering*, *26*(4), 447–452. doi: https://doi.org/10.1109/48.972077

Wenegrat, J. O., Callies, J., & Thomas, L. N. (2018). Submesoscale baroclinic instability in the bottom boundary layer. *Journal of Physical Oceanography*, *48*(11), 2571–2592. doi: https://doi.org/10.1175/JPO-D-17-0264.1

Wenegrat, J. O., & Thomas, L. N. (2020). Centrifugal and symmetric instability during Ekman adjustment of the bottom boundary layer. *Journal of Physical Oceanography*, *50*(6), 1793–1812. doi: https://doi.org/10.1175/JPO-D-20-0027.1

Wüest, A., Piepke, G., & Van Senden, D. C. (2000). Turbulent kinetic energy balance as a tool for estimating vertical diffusivity in wind-forced stratified waters. *Limnology and Oceanography*, *45*(6), 1388–1400. doi: https://doi.org/10.4319/lo.2000.45.6.1388

References in the Supporting Information

(Not cited in the main text)

Merckelbach, L. (2018). Initial release of Glider flight model. Version 1.0.1. Zenodo. doi: https://doi.org/10.5281/zenodo.2222694